THESIS

ON MODELED AND OBSERVED WARM RAINFALL OCCURRENCE AND ITS RELATIONSHIPS WITH CLOUD MACROPHYSICAL PROPERTIES

Submitted by

Joshua Matthew King

Department of Atmospheric Science

In partial fulfillment of the requirements

For the Degree of Master of Science

Colorado State University

Fort Collins, Colorado

Spring 2014

Master's Committee:

Advisor: Christian Kummerow
Co-Advisor: Susan van den Heever

Branislav Notaros

ABSTRACT

ON MODELED AND OBSERVED WARM RAINFALL OCCURRENCE AND ITS RELATIONSHIPS WITH CLOUD MACROPHYSICAL PROPERTIES

Rainfall from low-level, liquid-phase ("warm") clouds over the global oceans is ubiquitous and contributes non-negligibly to the total amount of precipitation that falls to the globe. In this study, modeled and observed warm rainfall occurrence and its bulk statistical relationships with cloud macrophysical properties are analyzed independently and directly compared with one another. Rain is found to fall from ~25% of the warm, maritime clouds observed from space by CloudSat and from ~27% of the warm clouds simulated within a large-scale, fine-resolution radiative convective equilibrium experiment performed with the Regional Atmospheric Modeling System (RAMS). Within both the model and the observations, the fractional occurrence of warm rainfall is found to increase with both column-integrated liquid water mass and cloud geometric depth, two cloud-scale properties that are shown to be directly related to one another. However, warm rain within RAMS is more likely with lower amounts of column water mass than observations indicate, suggesting that the parameterized cloud-to-rain conversion processes within RAMS produce rainfall too efficiently.

To gain insight into the relationships between warm rainfall production and the concentration of liquid water within a cloud layer, warm rainfall occurrence is subsequently investigated as a joint, simultaneous function of both cloud depth and column-integrated water mass. While rainfall production within RAMS is largely governed

by the availability of liquid water within the cloud volume, rain from observed warm clouds with relatively little column water mass is actually more likely to fall from deeper clouds with lower cloud-mean water contents. The latter, CloudSat-derived trend is shown to be robust across different seasons and environmental conditions; it varies little when the warm cloud distribution is stratified into ascending (day) and descending (night) CloudSat overpass groups. Using temperature differences between RAMS cloud tops and their immediate, surrounding environments as a proxy for cloud-top buoyancy, an attempt is then made to quantitatively investigate simulated warm rain occurrence within the broader context of cloud life cycle. It is found that rainfall likelihoods from RAMS-simulated warm clouds with cloud top temperatures warmer than their surrounding environments more closely resemble the overall CloudSat-derived rainfall occurrence trends. This result suggests that the CloudSat-observed warm cloud distribution is characterized by increased numbers of positively buoyant, developing clouds.

ACKNOWLEDGEMENTS

The ideas and analysis presented within this document represent the culmination of countless hours of great effort and diligence, a significant proportion of which were graciously contributed by others. I would be highly remiss if I did not pause to express my gratitude for this assistance. I first thank my advisors, Christian Kummerow and Susan van den Heever, for their unwavering support and sound scientific, professional and personal guidance throughout my time at Colorado State University. My development as a student-scientist stands as a testament to their superior mentorship. I also thank my committee member, Dr. Branislav Notaros, who graciously agreed to assume this role when circumstances forced Dr. Viswanathan Bringi to relinquish this responsibility. Special gratitude is extended to Dr. Greg Elsaesser, Dr. John Haynes and Matthew Igel for enlightening discussions on the nature of clouds and precipitation and our collective ability to characterize these systems using observations and models. Members of the Kummerow and van den Heever research groups provided additional and immeasurable technical guidance that greatly improved the quality of this research. Finally, I thank my family for their constant encouragement and support. It is an absolute fact that the completion of this work would not have been possible without the unconditional love provided by my wife, Meagan, to whom I am greatly indebted. This work was supported by the National Aeronautics and Space Administration under Grant NNX11AF06G and by the National Science Foundation under Grant AGS-1005316.

TABLE OF CONTENTS

CHAPTER 1: INTRODUCTION

1.1 Motivation

Low-level, liquid-phase ("warm") clouds cover vast portions of the global oceans and play a critical role in the global energy balance. Varying in form from temporally persistent stratocumulus decks only a few hundred meters thick to transient trade wind cumulus clouds with depths approaching 3-4 km, these clouds are commonly found in regions characterized by large-scale atmospheric subsidence. Low-level clouds are prevalent over the oceans (e.g., Mace et al. 2007; Medeiros et al. 2010); stratocumulus clouds alone cover approximately 23% of the ocean surface (Wood 2012). Due to their prevalence, and the fact that these clouds reflect large amounts of incoming solar radiation back to space while emitting longwave radiation at a temperature similar to that of the earth's surface, low-level clouds account for a large negative cloud radiative forcing (e.g., Hartmann et al. 1992). In this way, warm clouds exert a cooling effect on earth's surface. How these clouds may respond to a changing climate remains a topic of active debate. Difficulty parameterizing warm clouds within climate models represents a large source of uncertainty for predictions of future climate (Bony and Dufresne 2005; Webb et al. 2006).

Rainfall from warm maritime clouds is not generally intense (typically a few mm/hr or less), but it is ubiquitous, and thus, contributes non-negligibly to the total amount of precipitation that falls over the globe. Using rainfall intensity information derived from the Tropical Rainfall Measurement Mission (TRMM) Precipitation Radar, Short and Nakamura (2000) estimated that precipitation from shallow maritime clouds (storm top heights ≤ 2-3 km) produced approximately 20% of the total precipitation detected over the tropical

oceans. Subsequent warm rainfall estimates from TRMM (Lau and Wu 2003; Liu and Zipser 2009) and CloudSat (Chen et al. 2011) have largely acted to corroborate the contribution estimate put forth by Short and Nakamura (2000). Locally, drizzle and light rainfall can be the dominant contributors to precipitation totals. For example, Rapp et al. (2013) estimated that drizzle from low clouds accounts for 70% of all precipitation that falls within the southeastern Pacific stratocumulus region.

Rainfall is also one pathway to the depletion of cloud water within the atmospheric column, and in this way, its occurrence effectively acts to regulate local cloud radiative effects. Model simulations of marine stratocumulus clouds, for instance, have indicated that drizzle acts to reduce the column-integrated liquid water mass within the cloud layer (Nicholls 1987; Savic-Jovic and Stevens 2008; Ackerman et al. 2009). This column-integrated liquid water mass is directly related to cloud visible optical depth and, thus, cloud albedo (e.g., Stephens 1978). Therefore, a reduction in column-integrated water mass through rainfall results in a locally less reflective cloud field (Savic-Jovic and Stevens 2008).

1.2 Remote sensing of precipitation from space

Much of our understanding of the distribution of precipitation characteristics over the globe has arisen since the advent of the satellite era. Previously, precipitation estimation techniques relied largely upon rain gauge observations. Oceans cover approximately 70% of Earth's surface, but the spatial density of surface rainfall observation sites characterizing these oceanic environments remains very low. As a result, rainfall information derived from these rain gauge networks alone is not sufficient to characterize the full global distribution of precipitation. The development of satellite remote sensing

technologies has afforded a more comprehensive view of the global character of precipitation. Nonetheless, sensor limitations and retrieval methodology uncertainties associated with these technologies still collectively act to inhibit a complete understanding of global precipitation. The aim of this short section is to provide a brief overview of the sensors and methodologies that have been developed to estimate precipitation from space. For a more technical and comprehensive overview of this topic, readers are referred to Stephens and Kummerow (2007).

Passive precipitation retrieval methodologies rely upon observations of either infrared or microwave emission to infer precipitation intensity. Based on the idea that higher cloud top heights and colder cloud-top temperatures should be associated with the most intense rainfall, early infrared-based methodologies made use of statistically tuned brightness temperature thresholds to retrieve precipitation properties (e.g., Arkin 1979; Lovejoy and Austin 1979). However, within this paradigm, precipitation from warm-topped boundary layer clouds is severely underrepresented; the infrared brightness temperatures associated with these clouds are often higher than these pre-defined threshold values.

More recent precipitation retrieval methodologies have relied upon microwave emission observations made by space-borne radiometers (e.g., Wilheit 1986; Kummerow 2001; Hilburn and Wentz 2008; Kummerow et al. 2011). However, the emission signal observed by passive microwave sensors is inherently representative of the cumulative amount of cloud and precipitation liquid water within the atmospheric column. In order to derive a rain rate estimate from this emission signal, microwave rainfall retrieval methodologies must first make an assumption about the ratio of cloud and rainwater that

exists within a given scene. While some schemes rely upon output from cloud-resolving models (Kummerow et al. 2001) or a database of previously observed precipitation profiles (Kummerow et al. 2011) to partition the emission signal into cloud and rainwater components, others rely upon observationally-estimated fixed cloud liquid water path thresholds to infer this ratio (Wentz and Spencer 1998). Uncertainties in the chosen liquid water path partitioning threshold within the latter technique may lead to substantial systematic biases in climatologies of both cloud water path (O'Dell et al. 2008) and rainfall (Hilburn and Wentz 2008). Lebsock et al. (2011) recently capitalized upon precipitation sensitivity differences between the Moderate Resolution Imaging Spectroradiometer (MODIS) and CloudSat to more rigorously estimate the true ratio of cloud and rainwater within shallow marine clouds. While rainwater was largely non-existent at low cloud liquid water path values, the ratio of rain-to-cloud water approached 1:2 when 500 g m^{-2} of cloud water was present.

Unlike radiometers, radars are active sensors, meaning that they transmit a pulse and measure the signal that is returned. The first precipitation estimates derived from a space-borne radar were made in 1997 with the launch of the 13.8-GHz TRMM Precipitation Radar (PR; Kummerow et al. 1998). Still operational as of late 2013, the PR has provided unprecedented insight into the intensity and vertical structure of precipitation within the tropics (equatorward of 36° latitude). However, with a minimum detectable signal of 17 dBZ, the PR is not able to detect the lightest end of the precipitation intensity spectrum (i.e., rates below ~0.7 mm/hr). Using ground-based radars on the atoll of Kwajalein on the eastern edge of the western Pacific warm pool, Schumacher and Houze (2000) noted that the PR undersamples weakly precipitating echoes and, thus, misses ~ 2.3% of the near-

surface rainfall. More recent estimates have suggested that the PR misses up to 10% of the total rain volume within the tropics due to light rainfall insensitivities (Berg et al. 2010).

Launched in 2006, the CloudSat Cloud Profiling Radar (CPR) was the first cloud radar to operate in space (Stephens et al. 2002). With a frequency of 94 GHz and a minimum detectable signal of -30 dBZ, the CPR is able to detect both clouds (Marchand et al. 2008) and light precipitation (L'Ecuyer and Stephens 2002; Matrosov 2007; Haynes et al. 2009; Mitrescu et al. 2010; Lebsock and L'Ecuyer 2011). In this way, profiles of cloud and light precipitation properties obtained from the CPR compliment the precipitation profiles observed by the TRMM PR. Rainfall incidence information within the present study is wholly derived from CloudSat. The CloudSat mission and its cloud and precipitation identification algorithms are discussed in more detail within Chapter 2.

1.3 Warm rain processes

A fundamental and oft-studied problem within the field of cloud physics is to explain how warm clouds produce precipitation-sized drops over the relatively short timescales observed within nature. While incipient cloud droplets initially grow through diffusion of water vapor onto their surfaces, the amount of time required for these droplets to grow to precipitation-sized drops through the same condensational growth mechanism alone is simply far greater than the observed lifetime of many warm, precipitating clouds (e.g., Rogers and Yau 1989; Jonas 1996). Instead, cloud water is converted to rainwater within warm clouds chiefly through the warm rain collision and coalescence process. Within this process, the liquid droplet spectrum in a cloud is initially broadened through cloud droplet self-collection (auto-conversion) and is subsequently further widened chiefly through

collisions between cloud droplets and larger, precipitation-sized hydrometeors (accretion) (e.g., Berry and Reinhardt 1974). Using multi-sensor satellite observations of warm clouds over the global oceans, Stephens and Haynes (2007) estimated that these collision and coalescence processes collectively act to produce rain on timescales ranging from 26 minutes to 3 hours.

Warm rain collision and coalescence processes within bulk microphysical schemes in cloud-resolving models and larger scale climate models are commonly parameterized through empirically-derived cloud-to-rain conversion rates. Kessler (1969) proposed that the rate of auto-conversion within a warm cloud is linearly related to local cloud water mass concentrations; in this view, rain water is produced at a specified rate through the auto-conversion process whenever cloud water concentrations (or cloud water mixing ratios) exceed some critical threshold value (e.g., Liu and Daum 2004). Subsequent modifications to this simple conceptualization focused on including droplet number concentration and droplet size functionalities (e.g., Manton and Cotton 1977). Despite their simplicity, variations of such schemes are still commonly used to represent warm rain coalescence processes within models (e.g., Grabowski 1998; Suzuki and Stephens 2009).

Model-derived warm rain statistics analyzed within this study are obtained from the Regional Atmospheric Modeling System (RAMS; Pielke et al. 1992; Cotton et al. 2003). Unlike the Kessler-type coalescence schemes described within the previous paragraph, the bulk microphysical scheme used within RAMS makes use of look-up tables pre-calculated from a detailed bin-resolving model to simulate the rate of change in cloud and rain mass and number concentrations due to collision and coalescence processes (Feingold et al. 1998). The advantage of this bin-emulating approach is two-fold; its use incorporates the

added complexity of bin-resolved microphysical processes while maintaining the computational efficiency of a bulk microphysical scheme. To better represent the observed bimodal distribution of cloud droplets, RAMS was recently equipped with a large cloud droplet (drizzle) hydrometeor mode (Saleeby and Cotton 2004), whose diameters presently span a range of 50 to 100 μm (Saleeby and van den Heever 2013). Previously within RAMS, auto-conversion acted to convert the small cloud droplet mode (diameters < 50 μm) directly to the rain category (diameters > 100 μm). The inclusion of the drizzle hydrometeor category essentially slows the transition of cloud water to rainwater within the model by requiring that small cloud droplet collisions must first produce drizzle drops.

Despite its sophistication, the microphysical scheme used within RAMS may still overestimate the rate at which cloud water is converted to drizzle and rainwater through warm rain processes. Suzuki et al. (2011) compared warm rain statistics derived from a large-scale, fine-resolution radiative convective equilibrium (RCE) experiment performed with RAMS to those observed over the global oceans from space by CloudSat and MODIS. Warm rain processes simulated with RAMS converted liquid water to rain in a manner more consistent with observations than did those simulated with a simpler, Kessler-type microphysical scheme within the Non-Hydrodstatic Icosahedral Atmospheric Model (NICAM). However, drizzle within RAMS was still produced more efficiently with less cloud water than was suggested by the observations.

1.4 Observed warm rain occurrence

In Section 1.1, it was noted that low-level clouds cover substantial portions of the tropical oceans and rainfall from these clouds contributes non-negligibly to global

precipitation totals. Given the prevalence of these clouds, one may then ask: *What percentage of warm clouds over the oceans produce rainfall?* An answer to this question has been sought for decades. For example, Byers and Hall (1955) used an aircraft-mounted radar to determine that the presence of rain within maritime, liquid-phase clouds was ubiquitous. These early results have motivated more recent field studies, such as the Rain in (shallow) Cumulus over the Ocean campaign (RICO; Rauber et al. 2007), where it was estimated that approximately 10% of the shallow cloud distribution produced rain (Nuijens et al. 2009; Snodgrass et al. 2009).

The advent of space-borne sensors and associated methodologies designed to retrieve cloud and precipitation properties has opened the opportunity to examine the fractional occurrence of warm rainfall on greater spatial and temporal scales. Due to its global coverage and unique sensitivity to both drizzle and light rainfall, CloudSat, in particular, has proven a useful tool to this end. Many recent studies have utilized CloudSat-derived rainfall incidence information to estimate the frequency of rainfall from warm clouds over the oceans (Haynes and Stephens 2007; Lebsock et al. 2008; Leon et al. 2008; Kubar et al. 2009; Chen et al. 2011; Suzuki et al. 2011; Rapp et al. 2013; Christensen et al. 2013). Kubar et al. (2009) examined CloudSat-identified warm clouds over the oceans and, based upon the drizzling and non-drizzling reflectivity distributions measured by Frisch et al. (1995), defined rain-containing ("drizzling") scenes as those in which the in-cloud maximum CloudSat reflectivities exceeded -15 dBZ. The geographic distribution of the fraction of rain-containing to total warm cloud counts shown in Figure 1.1a highlights the ubiquity of rainfall production within warm, oceanic clouds. Over the central and eastern Pacific Ocean, up to 80% of the identified warm clouds contained drizzle or rain

hydrometeors within their volumes. However, the authors noted that using a maximum cloud reflectivity threshold to define drizzling or lightly raining scenes did not necessarily guarantee that precipitation hydrometeors within these scenes were reaching the ocean surface. Taking a more conservative approach, Lebsock et al. (2008) defined raining scenes as having CloudSat-identified cloud base reflectivities > 0 dBZ and accounted for warm clouds undetected by CloudSat (cloud tops obscured by surface contamination and/or low reflectivities), but observed by MODIS, to estimate that only 6.5% of warm clouds over the oceans certainly produced rainfall.

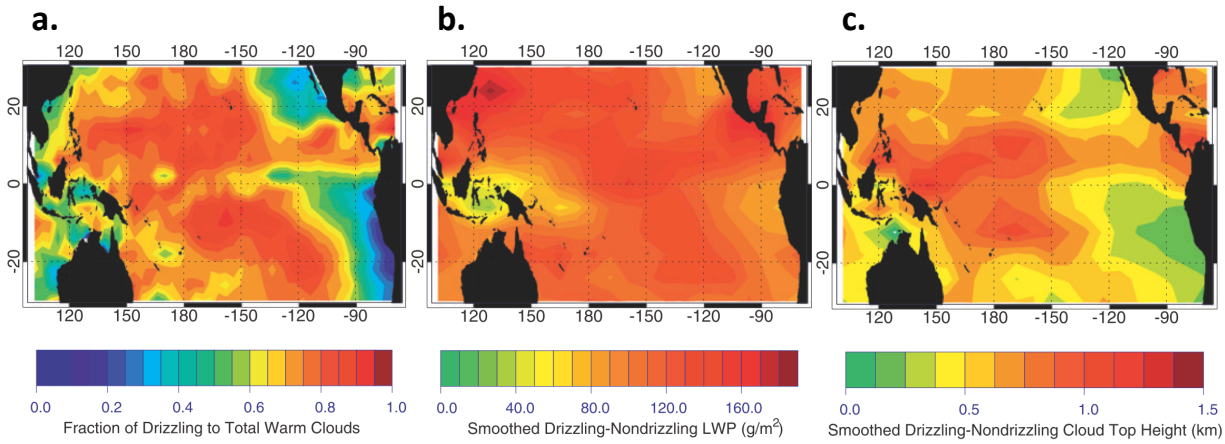

Figure 1.1. (a) Geographic distribution of the fraction of warm clouds that contained maximum CloudSat reflectivities > -15 dBZ ("drizzling"). The difference between drizzling and non-drizzling (b) liquid water path (LWP) and (c) cloud top height. From Kubar et al. (2009).

Another question that is often asked is: *Which warm cloud characteristics are most strongly associated with rainfall production?* Previous studies have shown strong links between a warm cloud's propensity to produce rainfall and a number of cloud macrophysical properties, the large-scale characteristics of the cloud itself. Two commonly retrieved cloud macrophysical variables are cloud top height (or cloud geometric depth) and cloud liquid water path, the column-integrated water mass within a cloud.

Observational evidence from both ground-based sensors (Zuidema et al. 2005; Rémillard et al. 2012) and space-borne sensors (Lebsock et al. 2008; Leon et al. 2008; Kubar et al. 2009; Chen et al. 2011; L'Ecuyer et al. 2011; Suzuki et al. 2011; Christensen et al. 2013) indicates that warm clouds with higher cloud liquid water paths are more likely to produce drizzle and rain. For example, Kubar et al. (2009) noted that cloud liquid water paths from drizzling warm clouds over the Pacific Ocean were often 100 g m^{-2} higher than those characterizing their non-drizzling counterparts (Figure 1.1b). Not unlike the simple warm rain coalescence parameterizations proposed by Kessler (1969), these findings suggest that these clouds are more likely to produce precipitation when increased amounts of cloud water are available for warm rain processes.

There is also a strong link between cloud depth and rain production within warm clouds (Byers and Hall 1955; Nuijens et al. 2008; Stephens et al. 2008; Kubar et al. 2009; Snodgrass et al. 2009; Reiche and Lasher-Trapp 2010; Rémillard et al. 2012; Christensen et al. 2013), as is exemplified in the drizzling and non-drizzling cloud top height differences shown in Figure 1.1c (Kubar et al. 2009). The exact reason for the existence of this relationship remains less clear but could be related to such key, and potentially interrelated, factors as liquid water availability and relative cloud age (e.g., Reiche and Lasher-Trapp 2010).

While not the focus of the present study, environmental factors and cloud microphysical characteristics (e.g., droplet sizes and number concentrations) also influence a warm cloud's propensity to produce rainfall. Satellite-derived evidence suggests that warm clouds developing within stable marine environments (high lower tropospheric static stability) rain more often at lower cloud liquid water paths than do warm clouds

within unstable marine environments (Lebsock et al. 2008; L'Ecuyer et al. 2009). As clouds within these stable environments are likely less vertically developed, the same amount of column water mass confined within these shallower clouds results in higher liquid water concentrations, which, in turn, promote more efficient warm rain processes. Lebsock et al. (2008) also noted that the probability of rainfall from warm, maritime clouds is positively correlated with column water vapor. The second aerosol indirect effect (Albrecht 1989) hypothesizes that when clouds form within environments characterized by high aerosol concentrations, their resulting cloud droplet size distributions contain increased numbers of smaller droplets, a cloud microphysical characteristic which would act to inhibit the broadening of the droplet size spectrum through warm rain collision and coalescence processes (Section 1.3). While high aerosol concentrations could potentially delay or ultimately prohibit the onset of rainfall, quantification of the relative impact of this effect on global cloud and precipitation properties is a topic of active debate. However, a growing amount of recent, satellite-derived evidence (e.g., Berg et al. 2008; Lebsock et al. 2008; L'Ecuyer et al. 2009; Kubar et al. 2009; Saleeby et al. 2010) largely supports the hypothesis put forth by Albrecht (1989). Collectively, the results from these studies suggest that cloud microphysical characteristics act to modulate the exact relationships between cloud macrophysical quantities and warm rain occurrence.

1.5 Overview

The principle aim of this study is to compare bulk statistical relationships between warm rainfall occurrence and cloud macrophysical properties observed by CloudSat to those simulated with RAMS. The two main cloud macrophysical properties examined

herein characterize warm cloud geometric depth and column-integrated water mass. The observed and modeled relationships between warm rainfall occurrence and these two cloud-scale properties are first investigated individually within Sections 4.1 and 4.2. To gain further insight into the relative importance of each factor in determining the statistical likelihood that a warm cloud produces precipitation, warm rainfall occurrence is subsequently investigated as a joint, simultaneous function of both cloud depth and column-integrated water mass within Section 4.3. As the latter step effectively involves constraining the same amount of column-integrated water to clouds of different depths, insight is gained into the relationship between rainfall probability and the concentration of liquid water within the cloud volume. Based on these findings, an attempt is then made within Section 4.4 to investigate the relative importance of cloud maturity, a previously unexplored metric, in determining the probability that clouds are producing rainfall at any given time.

The choice to use CloudSat observations to identify cloud and precipitation properties within this study was motivated by three key characteristics of the CloudSat mission itself. The first is related to CloudSat's ability to detect hydrometeors over the entirety of the globe. Non-negligible populations of low, and potentially warm, clouds exist over the oceans in the mid-latitudes (e.g., Mace et al. 2007); these clouds go undetected by space-borne sensors in a lower inclination orbit. Secondly, the CloudSat CPR is the first space-borne sensor capable of providing vertical profiles of cloud hydrometeor properties, and these observations were of critical importance to this study's cloud geometric property – warm rainfall occurrence comparison initiatives. Lastly and most importantly, the CPR's low minimum detectable threshold (approximately -30 dBZ) allows for the unique

detection of both cloud hydrometeors and light rainfall. Given this sensitivity, CloudSat is well-suited to observe the onset of precipitation within clouds, and thus, provide insight into the problem of cloud and rainwater partitioning discussed within Section 1.2.

The comparison of CloudSat-observed relationships between cloud macrophysical properties and warm rainfall occurrence to those simulated within RAMS was designed to be mutually beneficial to the remote sensing and atmospheric modeling communities. Models can be used to provide information about variables that are difficult to remotely sense, and, in this way, may be used to gain insight into the processes active within the observed cloud fields. With its sophisticated cloud microphysical scheme (Saleeby and van den Heever 2013), RAMS effectively represents the current state-of-the-art in mesoscale atmospheric modeling. Therefore, if care is taken to allow for fair comparisons between warm clouds simulated with RAMS and those observed by CloudSat, any pervasive differences in warm rainfall occurrence that exist between these two data sources likely indicate shortcomings in the current state of model representations of warm rain processes. Conversely, identifying these same potential differences would act to highlight the type of observations needed to constrain uncertainties in the current generation of warm rain collision and coalescence parameterizations.

CHAPTER 2: DATA SETS

2.1 CloudSat mission overview

The main observational datasets used throughout this study are derived from CloudSat (Stephens et al. 2002). Launched into a sun-synchronous orbit at an altitude of 705 km by the National Aeronautics and Space Administration (NASA) in April 2006, the main goal of the CloudSat mission was to obtain radar observations of the vertical structure of clouds and precipitation over the globe from space. Such measurements were of fundamental importance at the time of launch, as prior global observations of clouds were only representative of either their column-integrated characteristics or their net top of atmosphere impact on outgoing radiative fluxes. CloudSat was launched into a larger, multi-national constellation of Earth-observing satellites called the Afternoon Constellation (A-Train; Figure 2.1). Sensors aboard satellite members of the A-Train are capable of observing a wide range of atmospheric characteristics; broadly, these sensors are tailored to monitor water vapor, cloud properties, precipitation characteristics, atmospheric aerosols, radiation, and chemistry. With all members of the A-Train following the same orbital track, passing over the equator at 1:30 AM and 1:30 PM local time within at least 15 minutes of one another, it is possible to combine CloudSat data with ancillary observations from other A-Train sensors to provide a more comprehensive characterization of the atmosphere.

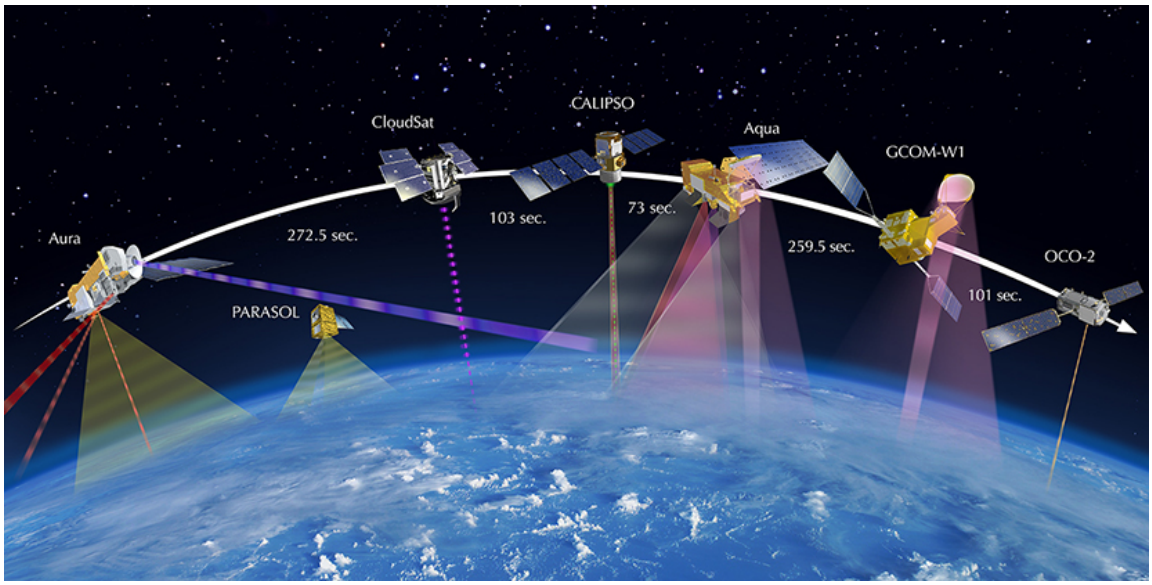

Figure 2.1. The A-Train constellation concept as of approximately early 2013. Times indicate separation between spacecraft. Note that at the Orbiting Carbon Observatory 2 (OCO-2) is scheduled for launch in July 2014. See Stephens et al. 2002 for descriptions of most other spacecraft and sensors. From the NASA Afternoon Costellation homepage (http://atrain.nasa.gov/taking.php).

The CloudSat mission flies the Cloud Profiling Radar (CPR), a nadir-pointing 94-GHz (W-band) radar (Im et al. 2005). With footprint dimensions of 1.7 x 1.3 km (along- and cross-track, respectively) and an effective vertical resolution of 480 m that is oversampled to 240 m vertical bins, each CloudSat orbit, or "granule", contains ~ 37,088 vertical reflectivity profiles (Figure 2.2). The CPR is not a scanning instrument; that is, it merely provides a two-dimensional, curtain-like measurement of reflectivity directly below CloudSat's orbital track. Though not the first space-borne radar tailored to take observations of the atmosphere (the Tropical Rainfall Measuring Mission (TRMM) precipitation radar (PR); Kummerow et al. 1998), the CPR provides a unique perspective on hydrometeor detection. Namely, whereas the 2.2-cm wavelength TRMM PR has a minimum detectable signal of approximately 17 dBZ and is thus not sensitive to clouds nor rain rates below 0.7 mm/hr, the 3.2-mm wavelength CPR has a minimum detectable signal

of approximately -30 dBZ, making it well suited to observe clouds and their transition to producing precipitation.

While CloudSat was launched in April 2006, data were not routinely collected and released until July 2006. Aside from small data gaps due to quality concerns, these data are available from July 2006 to April 2011 in a fully processed state. On April 17, 2011, CloudSat experienced a battery anomaly, the CPR stopped collecting data, and the spacecraft lost its position in the A-Train. While daytime-only observations were resumed on October 27, 2011, CloudSat did not re-enter the A-Train until May 15, 2012 (new position in A-Train shown in Figure 2.1). Unless otherwise noted, the CloudSat results presented within this analysis are derived from the July 2006 – April 2011 data record (~ 4.75 years).

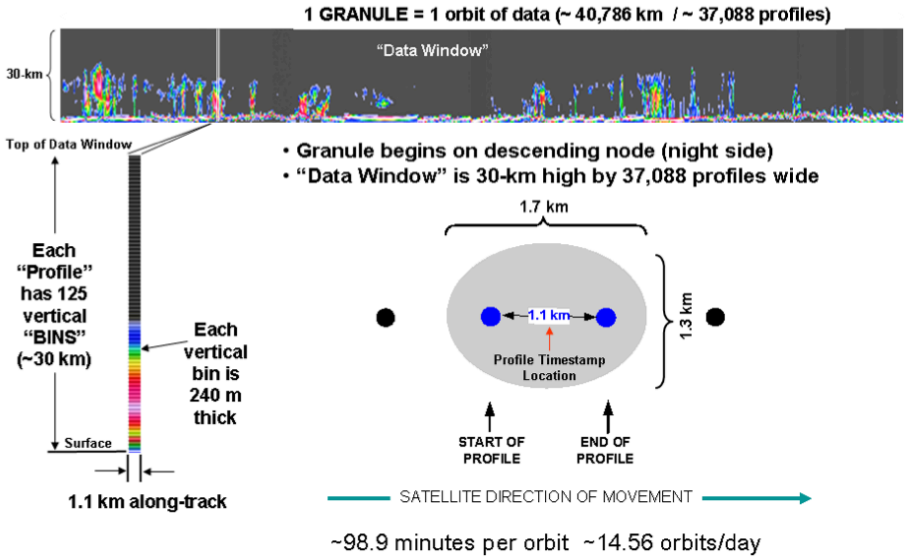

Figure 2.2. Schematic of a single CloudSat granule. Included are characteristics of the CPR's vertical and horizontal resolutions. From the CloudSat Standard Data Products Handbook (2008) (http://www.cloudsat.cira.colostate.edu/cloudsat_documentation/CloudSat_Data_Users_Handbook.pdf).

2.2 CloudSat 2B-GEOPROF product description

The raw measurement from CloudSat's CPR is that of returned power from the initial transmitted radar pulse. Thus, a first step in interpreting these data is to separate out radar noise from the desired returned power from scattering by cloud and precipitation hydrometeors. To this end, a CloudSat hydrometeor detection algorithm was developed (Marchand et al. 2008). The basic premise of the algorithm is to compare the magnitude of the estimated radar noise power to that of the raw power that remains once this noise power has been subtracted from the observed signal. As the latter power – referred to as the target power – becomes increasingly larger than threshold values of the standard deviation of noise power in a given vertical bin, there is increasing likelihood that scattering hydrometeors exist in the bin.

Operationally, this algorithm is used to produce the cloud mask in the CloudSat Geometrical Profiling Product (2B-GEOPROF). Based on the results from the algorithm described above, each vertical bin in a given CloudSat profile is assigned a cloud mask value indicating the likelihood that the vertical bin contains hydrometeors. Generally, as cloud mask values increase from 10 (very weak echo) to a maximum of 40 (strong echo), the percentage of possible false hydrometeor detections decreases from less than 50% to less than 0.2% (Marchand et al. 2008). At a cloud mask value of 20 (weak echo), while the original mission goal percentage of false hydrometeor detections was less than 16%, comparisons with Cloud-Aerosol Lidar and Infrared Pathfinder Satellite Observation (CALIPSO) observations indicate that this percentage may be as low as 5%. At the CPR's 94-GHz frequency, the surface is roughly two to five orders of magnitude more reflective than hydrometeors within a CloudSat profile. As a result, surface radar returns dominate the

lowest CloudSat vertical bins, typically contaminating the first three bins nearest to the surface (or, up to at an approximate altitude of 720 m). In the operational algorithm, very strong returned power near the surface is identified as likely surface clutter, and the cloud mask for corresponding vertical bins is given a value of 5 to flag this likely contamination. Thus, while very shallow, near-surface clouds that are completely obscured by this surface clutter may be numerous (e.g., Lebsock et al. 2008), no attempt is made to account for them within the present analysis.

An example of the relationship between CPR reflectivity and the 2B-GEOPROF cloud mask for one portion of a single orbit is shown in Figure 2.3. The given scene is characterized by a large area of vertically deep, high reflectivity returns in its early portions and a number of shallower, weaker returns further along CloudSat's ground track. A radar bright band associated with the melting of frozen hydrometeors is evident at an approximate altitude of 3 km, providing a rough estimate for the freezing level in the scene. Given that many of the radar returns extend well above this altitude, both liquid and frozen hydrometeors are likely present in the sampled volume. The corresponding 2B-GEOPROF cloud mask for the scene closely resembles the reflectivity field; as higher CPR reflectivities indicate increasing amounts of scattering from hydrometeors, this behavior is to be expected. Regions of high reflectivity are associated with the maximum cloud mask value of 40 (red in Figure 2.3b) to indicate the greatest confidence that these regions contain hydrometeors. The high reflectivities in the vertical bins closest to the surface are interpreted by the algorithm as surface clutter and are given a cloud mask value of 5 (dark purple in Figure 2.3b).

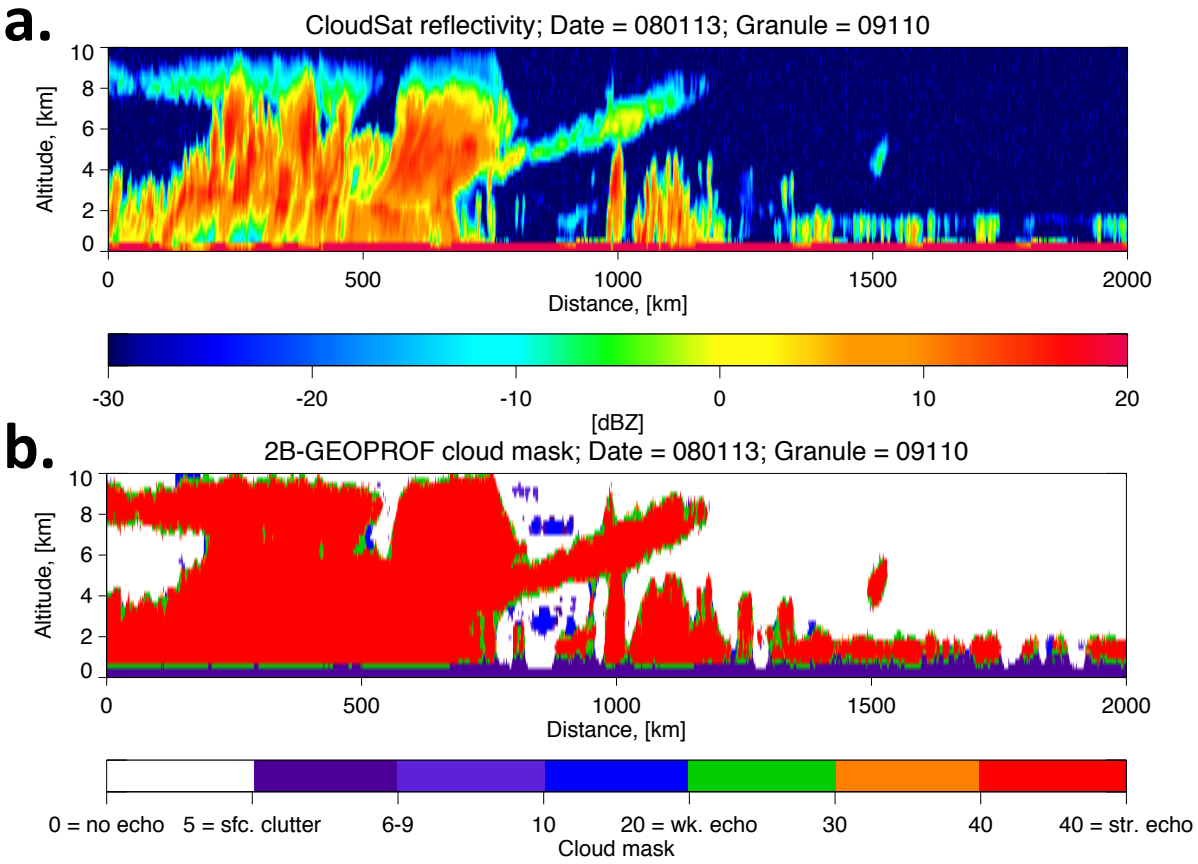

Figure 2.3. (a) CloudSat reflectivity and (b) 2B-GEOPROF cloud mask for one portion of the same orbit. See Marchand et al. (2008) for a more detailed description of the CloudSat cloud mask.

2.3 CloudSat 2C-PRECIP-COLUMN product description

As was noted in Section 2.1, one primary goal of the CloudSat mission was to facilitate climatologies of light precipitation. To this end, a number of schemes have been specifically developed to estimate rainfall from CloudSat CPR returns. Utilizing an optimal estimation approach, L'Ecuyer and Stephens (2002) introduced a method for retrieving rainfall characteristics from CPR reflectivity profiles, with an added constraint on path-integrated attenuation, the two-way extinction of the radar pulse as it propagates through

the atmospheric column. At the CPR's 3.2-mm wavelength, attenuation of the radar beam can be significant, increasing as rain rate increases and becoming severe at rain rates above approximately 1.5 mm hr^{-1}. While this effect limits the ability to derive meaningful quantitative estimates of rainfall from CloudSat, L'Ecuyer and Stephens (2002) found that the use of path-integrated attenuation as an added constraint in their rainfall retrieval algorithm – thereby utilizing this attenuation as a useful signal – allowed for acceptable rain rate estimates to the 5-8 mm hr^{-1} range. Matrosov (2007) employed a slightly different attenuation-based approach for deriving rain characteristics from CloudSat, wherein the vertical gradient of observed CPR reflectivity was used to estimate an attenuation coefficient profile. This attenuation estimate was then used to estimate rainfall characteristics in the profile through the use of an experimentally-derived relationship between this attenuation coefficient and rain rate.

Following upon these attenuation-based methodologies, Haynes et al. (2009) developed another technique for deriving precipitation incidence and intensity from CloudSat observations. Forming the basis for the operational CloudSat 2C-PRECIP-COLUMN product, this algorithm employs an alternative approach for estimating path-integrated attenuation. As was mentioned previously, the surface is much more reflective than hydrometeors at the 94-GHz frequency of the CPR. Thus, any reduction in the observed backscatter from the expected surface value in a given scene is indicative of attenuation of the radar beam within the atmospheric column. In the 2C-PRECIP-COLUMN algorithm, the path-integrated attenuation due only to hydrometeors (hereafter referred to as PIA) is given by

$$PIA = \sigma_{clr} - (\sigma_0 - G),$$

where σ_{clr} is the clear sky, non-attenuated normalized backscattering cross section of the surface, σ_0 is the observed normalized backscattering cross section of the surface, and G is the two-way attenuation due to atmospheric gases. In the algorithm, G is estimated by using temperature and water vapor profiles provided from auxiliary ECMWF data matched to the CloudSat scenes.

To estimate σ_{clr}, ancillary information about the scene's underlying surface is needed. As this parameter varies greatly in response to differing land surface characteristics (vegetation, slope of terrain, snow cover, etc.), no estimates of σ_{clr}, PIA or rainfall are made over land in the 2C-PRECIP-COLUMN algorithm. Over the ocean, σ_{clr} is much less variable, with chief dependencies upon surface wind speed (surface roughening) and sea surface temperature (SST). To determine the relative importance of these two dependencies, an empirical relationship between CloudSat σ_{clr}, wind speeds derived from AMSR-E, and ECMWF SSTs was developed for use in the algorithm.

Table 2.1. CloudSat 2C-PRECIP-COLUMN rainfall incidence flag descriptions and associated near-surface, unattenuated reflectivity (Z_u) values. From Haynes et al. (2009).

Rainfall incidence	**Associated Z_u range, (dB)**
Rain certain	$Z_u > 0$
Rain probable	$-7.5 < Z_u < 0$
Rain possible	$-15 < Z_u < -7.5$
No rain	$Z_u < -15$

To determine precipitation incidence and intensity in a given CloudSat scene, the 2C-PRECIP-COLUMN algorithm uses this estimate of PIA in conjunction with CPR reflectivity information. The objective of the algorithm is to estimate surface rainfall characteristics, but as was previously noted, the reflectivity in the CloudSat range gates

nearest to the Earth's surface are contaminated by surface clutter. Thus, surface rainfall characteristics must be implied from the fourth bin above the surface, at an approximate altitude of 720 m. The observed near-surface reflectivity at this level (Z_{ns}) is added to the PIA estimate at the near-surface level to obtain the near-surface, unattenuated reflectivity (Z_u). Rainfall incidence in a given scene is then determined by comparing Z_u to the threshold values given in Table 2.1. In general, as Z_u increases, near-surface rainfall becomes increasingly more likely. While additional, independent precipitation intensity estimates are calculated in the CloudSat 2C-RAIN-PROFILE product (Mitrescu et al. 2010; Lebsock and L'Ecuyer 2011), both CloudSat precipitation retrieval algorithms rely upon precipitation incidence information from the 2C-PRECIP-COLUMN product.

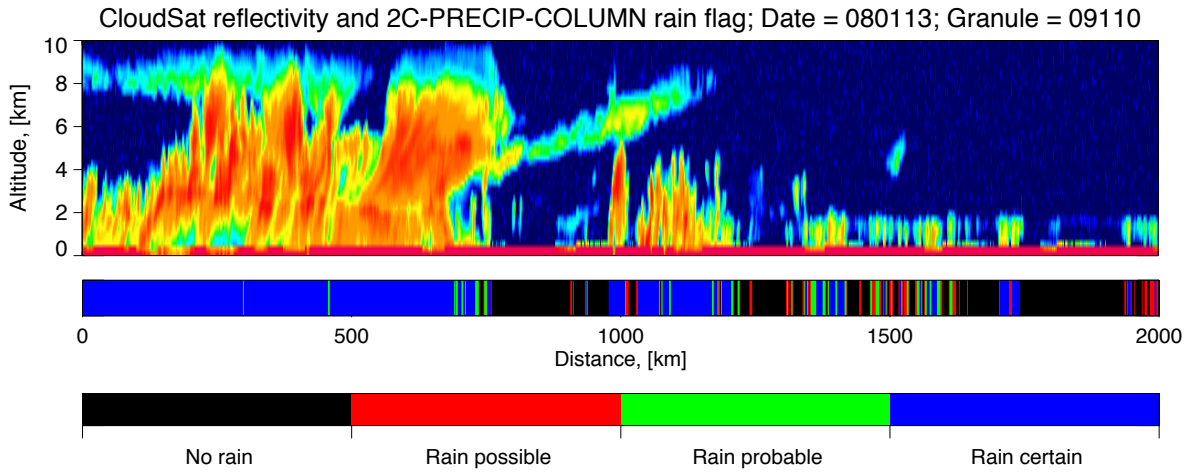

Figure 2.4. CloudSat reflectivity (top) and the corresponding 2C-PRECIP-COLUMN rainfall incidence flag (bottom) for the same CloudSat orbit portion plotted in Figure 2.3.

Figure 2.4 displays rainfall incidence information from the 2C-PRECIP-COLUMN product for the same portion of the CloudSat orbit plotted in Figure 2.3. The large area of vertically deep, high reflectivity returns (top) flanking the left-hand portion of the scene is largely flagged as certainly raining (blue, bottom) by the 2C-PRECIP-COLUMN algorithm. While a high-based cloud does exist at altitudes above ~ 5 km approximately 800 km from

the beginning of the scene (Figure 2.3b), near-surface reflectivities beneath this cloud are low, and, thus, the region is flagged as non-raining (black). The shallower radar returns within the right-hand portion of the scene are characterized by a variety of rainfall classifications; some of the clouds are identified as certainly raining, while others were marked as less likely to have been producing rainfall.

In this study, 2C-PRECIP-COLUMN data are used to characterize both rainfall incidence and PIA for CloudSat scenes. No effort is made to exclude scenes with negative PIA estimates from this analysis. While non-physical, PIA values below 0 dB result from uncertainties in the estimation of σ_{clr}, and are, in reality, likely representative of small positive PIA values (J. Haynes 2013, personal communication). Ancillary sea surface temperature (SST) data and profiles of atmospheric temperature for the CloudSat scenes are provided from the CloudSat ECMWF-AUX product (P. Partain, CloudSat ECMWF-AUX Auxiliary Data Process Description and Interface Control Document, 2007, http://www.cloudsat.cira.colostate.edu/dataICDlist.php?go=list&path=/ECMWF-AUX).

2.4 Mesoscale model simulations

Mesoscale model data for this study are derived from the Regional Atmospheric Modeling System (RAMS) (Pielke et al. 1992; Cotton et al. 2003). Conceived and refined at Colorado State University, RAMS is a non-hydrostatic, regional cloud-resolving model that has been used to simulate meteorological events on scales and levels of complexity ranging from sea breeze circulations (Darby et al. 2002) to supercell thunderstorms (van den Heever and Cotton 2004) to the North American Monsoon (Castro et al. 2007). RAMS data serve two main purposes in this study. First, as a model can provide insight into cloud

processes and environmental characteristics that are difficult to accurately observe on a large scale in the real world (e.g., vertical velocity, hydrometeor number concentration), RAMS was used to effectively supplement the CloudSat data, facilitating more comprehensive interpretations of observationally-derived results. Secondly, it was of interest to compare the rainfall incidence characteristics of warm clouds observed by CloudSat with those represented by RAMS to both highlight and assess any pervasive differences between the two independent data sets.

To adequately evaluate the characterization of rainfall from warm clouds within RAMS and compare this representation to CloudSat observations, a large, RAMS-derived statistical sample was needed at a spatial resolution comparable to that of CloudSat (Figure 2.2). In order to satisfy these requirements, pre-existing RAMS output from a large-domain, fine-resolution radiative-convective equilibrium (RCE) experiment described by Igel and van den Heever (2013) were analyzed. Initialized from a sounding characteristic of the mean tropical atmosphere, the simulation was run for 70 days, reaching a state of equilibrium at day 30. A number of simulations operating under conditions of RCE have previously been used to successfully study the characteristics of tropical clouds (e.g., Stephens et al. 2008; van den Heever et al. 2011; Storer and van den Heever 2013).

Pertinent characteristics of the RCE simulation are summarized in Table 2.2. The channel-like model domain is comprised of 3000 x 200 grid points in the zonal and meridional directions, respectively, with a 1-km horizontal grid spacing that is comparable to the footprint dimensions of a CloudSat pixel (Figure 2.2). The 26-km deep domain is represented by 65 vertical levels that range in depth from 70 m (at the surface) to 750 m (at domain top). The simulation uses a two-moment, bin-emulating bulk microphysical

scheme (Meyers et al. 1997) that predicts both mixing ratio and number concentration for eight different hydrometeor species (Saleeby and Cotton 2004). Pertinent to the warm cloud focus of this study, liquid hydrometeors within RAMS are represented by cloud droplet, drizzle and rain specie categories (Saleeby and van den Heever 2013). The SST of the underlying ocean surface is set to 300 K. Where appropriate, the full CloudSat data record is constrained to profiles observed over an SST of 300 K to support this study's model-observation comparison initiatives.

For this study, hourly RAMS output from the final three weeks of the simulation were analyzed. Before any screening of this RAMS data was performed, a total of more than 316 million grid boxes at a 1 km^2 horizontal resolution were available for analysis.

Table 2.2. RAMS radiative-convective equilibrium (RCE) simulation characteristics. For a more complete description of this simulation, see Igel and van den Heever (2013).

Horizontal domain characteristics	3000 x 200 grid points (1-km grid spacing)
Vertical domain characteristics	65 grid points (variable grid spacing); domain extending to an altitude of 26 km
Microphysical scheme	Two-moment, bin-emulating bulk scheme
Hydrometeor species	8 in total (cloud, drizzle, rain, pristine ice, snow, aggregates, graupel and hail)
SST	Fixed at 300 K
Incoming solar radiation	Fixed at 450 Wm^{-2}
Aerosol	Fixed (height and time) at 100 cc^{-1}

CHAPTER 3: METHODS

3.1 Determination of observed cloud geometric properties

A first step in this analysis was to determine basic, geometric properties of the clouds observed by CloudSat. These characteristics were derived from the CloudSat 2B-GEOPROF product (see Section 2.2). For this analysis, clouds layers in the CloudSat profiles were defined as having a 2B-GEOPROF cloud mask value greater than or equal to 20. At this cloud mask value, the percentage of false hydrometeor detection is low (~5%; Marchand et al. 2008). Vertically consecutive cloudy CloudSat range bins – and the heights of these range bins – were used to determine cloud echo top and base heights within the observed profiles. For any given cloudy layer within a profile, cloud echo top (base) height was simply defined as the highest (lowest) cloudy range bin within the cloud layer. Figure 3.1 shows the lowest cloud echo top (blue) and base (red) heights identified through this methodology for the same CloudSat field plotted in Figure 2.3. It should be noted that the surface clutter regions of all CloudSat profiles (yellow in Figure 3.1) are, by default, designated as non-cloudy through the application of the chosen cloud mask definition. Thus, in the case that clouds in the given CloudSat scene actually extend into these lowest range bins, the scene's cloud echo base is inevitably defined as the lowest clutter-free range bin.

Multiple cloud layers were often identified through the application of this methodology, sometimes totaling 4 or 5. While these multi-layered clouds often produce precipitation (e.g., Stephens and Wood 2007; Stephens et al. 2008), they complicate the interpretation of column-integrated quantities, such as PIA. For example, the PIA for a

profile with two cloud layers represents the cumulative attenuation from each of the cloud layers. Column-integrated quantities for single cloud layers, on the other hand, are directly representative of the characteristics of that single cloud layer. Thus, in order to directly examine the relationships between cloud geometric characteristics and cloud attenuation properties, the analysis was restricted to scenes containing single cloud layers.

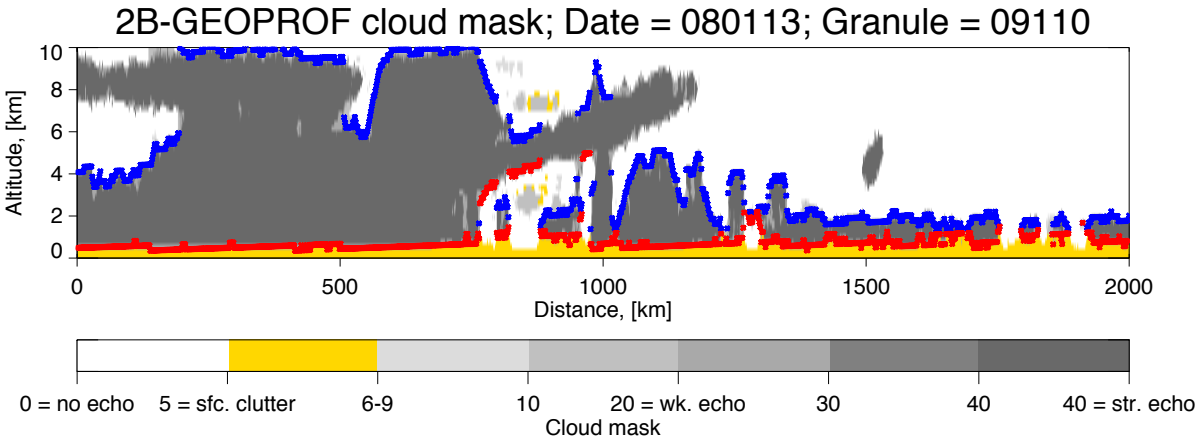

Figure 3.1. Lowest identified cloud echo top (blue) and base (red) heights plotted over the 2B-GEOPROF cloud mask (greyscale) for the same CloudSat orbit portion plotted in Figure 2.3. Cloud layers within the CloudSat profiles are defined where 2B-GEOPROF cloud mask values exceed 20.

As the focus of this study is on rainfall from liquid-phase clouds, a method was needed to further restrict the analysis to clouds with echo tops below the freezing level. To this end, an estimate of freezing level height, calculated from ECMWF-AUX temperature profile information, was available through the 2C-PRECIP-COLUMN product. Liquid-phase ("warm") clouds were then defined as having tops with heights at or below the corresponding freezing level height estimates. This screening step was performed to ensure that – within the bounds of the uncertainty in the freezing level height estimate – direct evaluations of the relationships between selected cloud characteristics and rainfall

could be made without interpretation of the added complexity of mixed-phase cloud microphysics. As very few entirely liquid-phase CloudSat scenes were detected at high latitudes, the entire analysis was restricted to scenes equatorward of 70°N/S latitude.

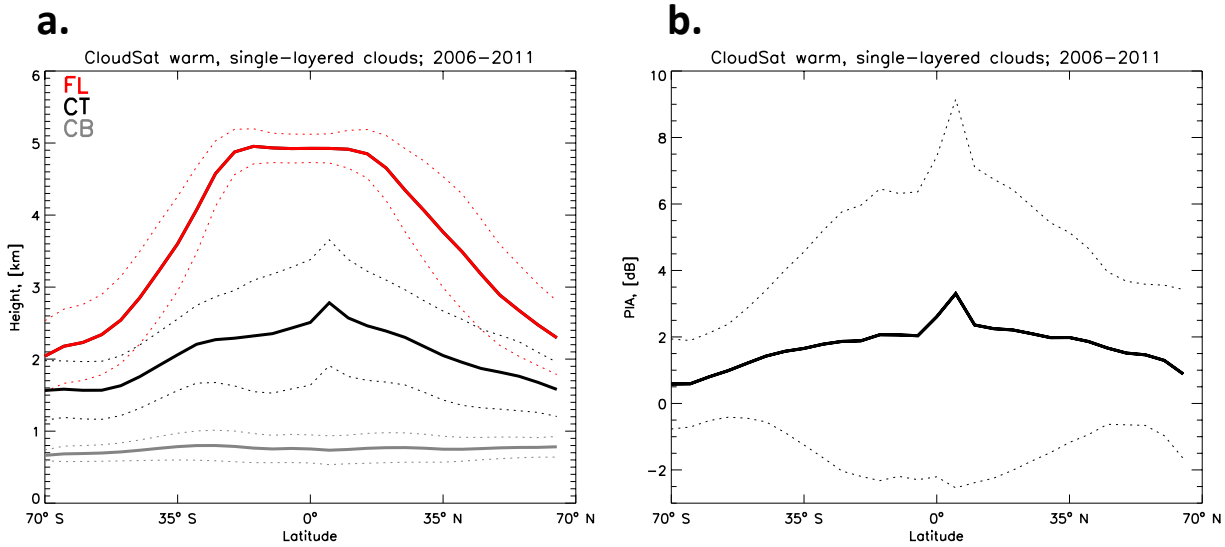

Figure 3.2. (a) Zonally averaged freezing level height (FL; red), cloud echo top height (CT; black) and cloud echo base height (CB; grey) for warm, single-layered clouds. (b) Zonally averaged PIA for the same cloud subset. For both plots, bold lines represent the zonal mean, and dotted lines represent the zonal standard deviations about the zonal mean.

Through the application of these two distinct screening requirements, the remaining CloudSat-derived distribution was composed only of warm, single-layered clouds. Over the full CloudSat data record (July 2006 – April 2011), this remaining distribution contained more than 23 million unique CloudSat profile observations of this cloud type. The zonal mean characteristics of this warm, single-layered core data set are shown in Figure 3.2. Large latitudinal variations exist in the height of the freezing level (FL; red), with peak zonal mean freezing level heights around 5km in the deep tropics (Figure 3.2a). The zonal mean cloud echo top heights (CT; black) mirror the latitudinal variation in freezing level height, with a maximum near the equator and minima at the poleward latitude extremes

considered in this analysis. As all clouds in this composite were required to have tops at or below the freezing level, the zonal mean cloud echo top heights fall well below the zonal mean freezing level at all latitudes. Zonal mean cloud echo base heights (grey) defined through this methodology vary little from the distribution's 770-m overall mean value. While this zonal consistency may in part be related to either surface clutter limiting CloudSat's ability to detect cloud bases located within the three lowest vertical range gates (below ~720 m) or rainfall obscuring actual cloud bases in precipitating scenes, direct observations of cloud base heights characterizing shallow maritime clouds during field campaigns such as RICO and the Atlantic Stratocumulus Transition Experiment (ASTEX) generally range between 400 and 1000 m (e.g., Wang et al. 1999; Zuidema et al. 2009; Reiche and Lasher-Trapp 2010; Remillard et al. 2012), lending some credibility to the CloudSat-derived estimates summarized in Figure 3.2a. Moreover, the mean lifting condensation level (LCL) calculated for this warm cloud distribution from ancillary ECMWF-AUX temperature and specific humidity fields was 570 m, a mere 200 m (or, the approximate depth of a single CloudSat vertical range gate) lower than the mean cloud echo base height identified through the present methodology.

The associated zonal mean PIA for these clouds (Figure 3.2b) generally mirrors latitudinal variations in cloud echo top height, indicating that deeper clouds act to attenuate the CPR radar beam to a greater degree than do shallower clouds. The relationships between PIA and cloud geometric properties will be explored more rigorously in later sections.

3.2 Delineation of raining and non-raining CloudSat scenes

The remaining warm, single-layered CloudSat scenes were categorized as either raining or non-raining through use of the 2C-PRECIP-COLUMN precipitation incidence flag (Section 2.3). For this analysis, raining scenes were defined as having a "rain certain" flag, whereas non-raining scenes could have either "no rain," "rain possible, " or "rain probable" flags (Table 2.1). While previous studies have chosen to interpret the "rain possible" and "rain probable" flags as collectively indicating the presence of drizzle (L'Ecuyer et al. 2009; Suzuki et al. 2011), the choice to only include the most certain rainfall flag in the raining definition was made to ensure that the scenes were, indeed, raining with the highest possible degree of confidence. Application of this raining and non-raining stratification on the total warm, single-layered cloud subset resulted in approximately 6 and 17 million raining and non-raining CloudSat scenes, respectively.

To gain an understanding of the spatial distributions of these warm, single-layered cloud subsets, the CloudSat scenes were binned into 5° x 5° grid boxes over the 70°N to 70°S study domain. Figure 3.3 shows the resulting mapped warm, single-layered raining and non-raining cloud counts. From these maps, it is apparent that many of the raining and non-raining counts originate from prominent subtropical stratocumulus cloud regions; the greatest density of counts was observed over the southeastern Pacific Ocean. As clouds in these stratocumulus regions are generally shallow and persistent in time, it is not surprising that many warm, single-layered clouds were observed in these locations. In general, most tropical and subtropical oceanic regions are well-represented (~1,000 total counts or more) in the distributions. However, scenes observed at the highest latitudes (greater than ~55°N/S) contribute comparatively little to the warm cloud distributions; as

the freezing level is, on average, at a lower altitude at these high latitudes (Figure 3.2), it is no surprise that relatively few clouds in these regions were observed to have cloud echo tops below the freezing level.

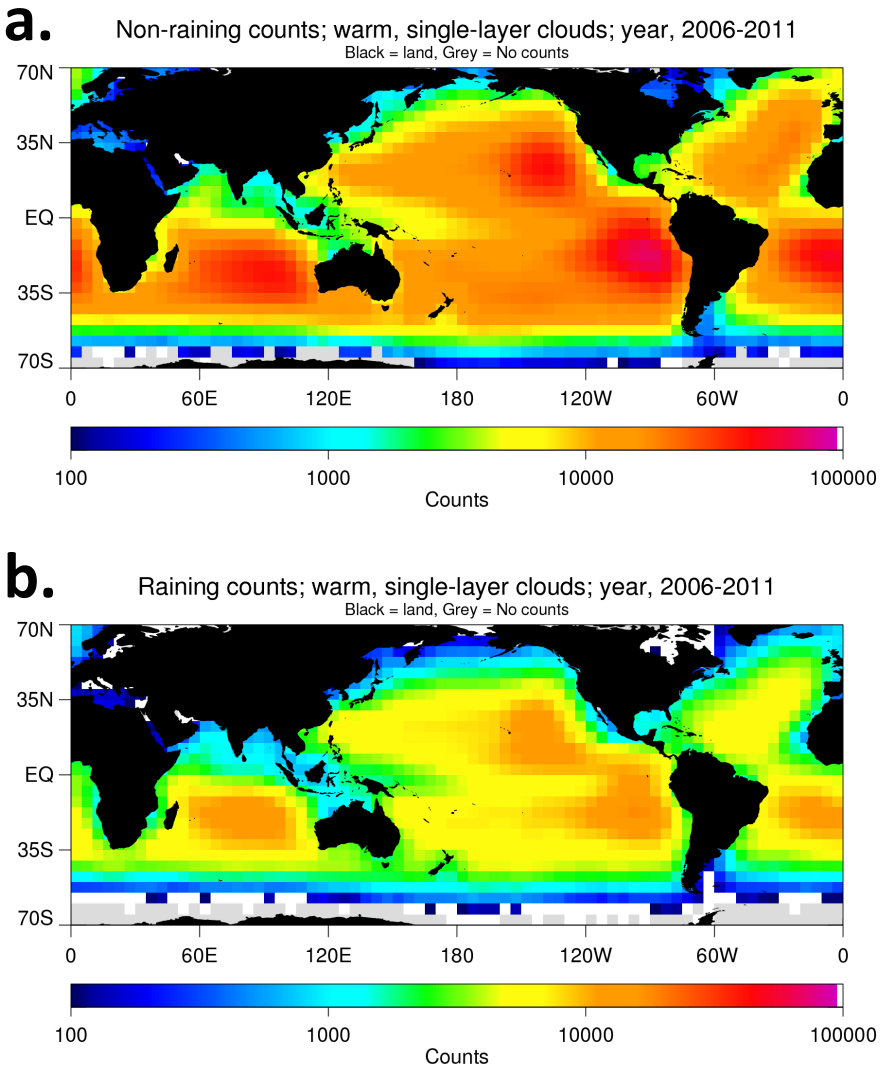

Figure 3.3. Maps of (a) non-raining and (b) raining warm, single-layered cloud counts over the entire available CloudSat record (2006-2011).

From comparison of the raining and non-raining counts in Figure 3.3, it is apparent that non-raining clouds outnumber raining clouds in any given location. In general, rain is a relatively rare phenomenon in this warm, single-layered cloud subset. Indeed, over the

entire 70°N to 70°S analysis region, raining scenes account for ~25% of the total warm, single-layered cloud distribution. While this value is higher than the 6.5% A-Train-derived estimate from Lebsock et al. (2008), the latter study made use of the MODIS to supplement CloudSat observations of warm clouds. Namely, MODIS observations were used to characterize warm clouds that either fell below CloudSat's -30 dBZ minimum detectable signal or were shallow enough to be completely obscured by surface contamination. As these MODIS-detected warm clouds were reportedly numerous and exclusively identified as non-raining, it is no surprise that the present, CloudSat-derived estimate of warm rain occurrence exceeds that of the aforementioned assessment.

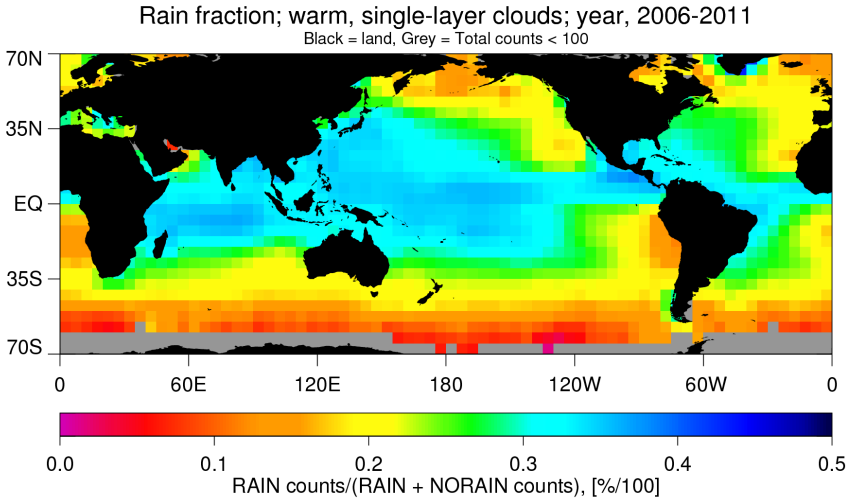

Figure 3.4. Map of the fraction of raining counts to total (raining and non-raining) counts in each grid box for the warm, single-layer cloud subset over the entire available CloudSat record (2006-2011).

Figure 3.4 shows the spatial distribution of the fraction of raining counts to total (raining and non-raining) counts (hereafter, "rain fraction"). While the warm, single-layered rain fraction generally exceeds the 25% average value throughout the majority of the tropical and subtropical oceanic regions, it is considerably lower than the mean in both

prominent stratocumulus cloud regions and the Northern and Southern Hemisphere storm tracks. When the analysis is restricted to warm, single-layered clouds associated with ECMWF-AUX SSTs within ±0.25 K of the 300 K value characteristic of the RAMS RCE simulation (Section 2.4), the rain fraction increases to 26.2%, marginally higher than the overall average value.

3.3 Processing mesoscale model data

Before direct comparisons between CloudSat-observed and RAMS-simulated warm clouds could be made, it was first desirable to use the RAMS output to compute simulated radar observables. To do so, all RAMS data were first processed with the QuickBeam radar simulator (Haynes et al. 2007). A frequency of 94 GHz was specified to model CloudSat's CPR. After this processing step was complete, simulated profiles of attenuation-corrected reflectivity and column PIA values from RAMS were available for comparison with those from CloudSat. To define consistent cloud boundaries for the RAMS data set, the relationship between the 2B-GEOPROF cloud mask (Section 2.2) and observed attenuation-corrected CPR reflectivities at all altitudes was investigated for both January and July of 2007 (Figure 3.5). The mean reflectivities associated with the cloud mask value of 20 used to define cloud boundaries in the CloudSat portion of this analysis were -26.0 and -25.8 for January and July of 2007, respectively. Based on these results, an attenuation-corrected reflectivity value of -26 dBZ was used to define cloudy portions of the RAMS domains. Accordingly, cloud base (top) height for a given cloud layer was defined as the lowest (highest) model level height within a vertically-consecutive block of model grid points whose simulated reflectivities exceeded this threshold value.

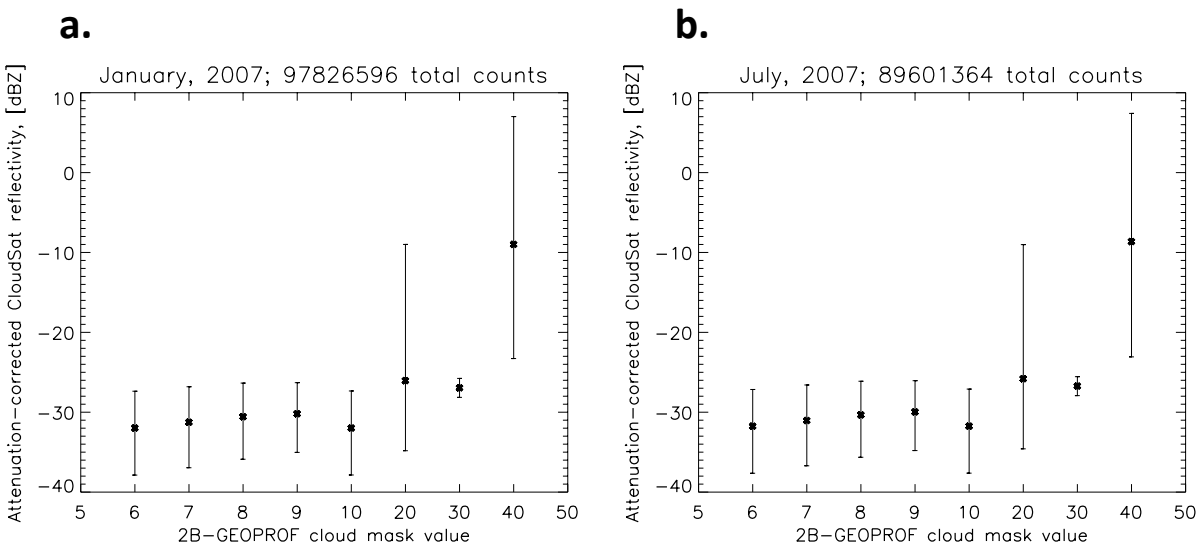

Figure 3.5. Relationship between CloudSat reflectivity and the 2B-GEOPROF cloud mask in all CloudSat vertical bins for (a) January, 2007 and (b) July of 2007. Bold points represent the mean reflectivity at each cloud mask value. The lower and upper bar points represent the 10th and 90th percentile reflectivity values, respectively.

These simulated radar data were used in conjunction with the CloudSat 2C-PRECIP-COLUMN algorithm (Section 2.3) to determine both the freezing level height and precipitation incidence within the RAMS domains. The same screening procedures outlined for CloudSat in Section 3.1 were used to isolate RAMS grid boxes that contained a single cloud layer with a top height at or below the freezing level height. Application of these screening procedures over the full three weeks of hourly RAMS simulation output resulted in the identification of approximately 72 million grid boxes that contained warm, single-layered clouds. While the size of this sample is larger than the 23 million warm, single-layered clouds observed by CloudSat over its full data record, both samples are thought to be sufficiently large enough to assess mean cloud and rainfall characteristics. Using the same rainfall definitions outlined in Section 3.2, the 2C-PRECIP-COLUMN precipitation incidence flag was then used to separate this warm, single-layered simulated cloud subset into raining and non-raining categories. A total of approximately 20 and 52 million warm,

single-layered raining and non-raining grid boxes, respectively, were identified. The fraction of raining counts to total warm, single-layered counts indicates that approximately 27% of the remaining distribution was identified as raining. This figure compares well with the 26.2% value obtained from the comparable fixed SST CloudSat data set (Section 3.2).

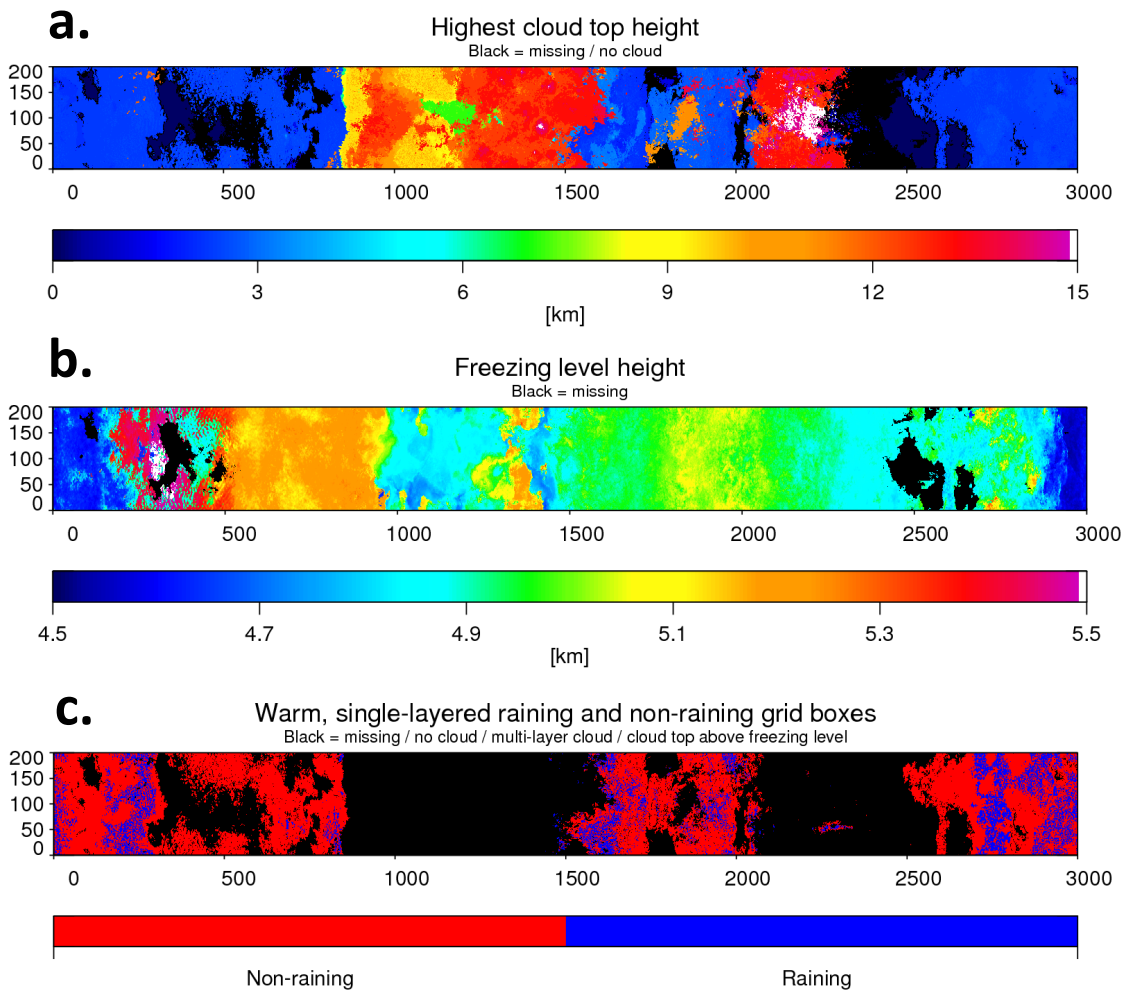

Figure 3.6. Example plan view images of the RAMS domain at a given time step. (a) Highest cloud top height. (b) Freezing level height. (c) Grid boxes containing a single cloud layer with a cloud top below the freezing level. Grid boxes containing these warm, single-layered clouds are separated into raining (blue) and non-raining (red) categories.

Plan view characteristics of an example RAMS domain are shown in Figure 3.6. As warm clouds are defined as having tops at or below the freezing level, portions of the

domain where the highest cloud top height (Figure 3.6a) exceeds the freezing level height (Figure 3.6b) are not considered for analysis. Grid boxes containing the remaining warm, single-layered cloud subset are highlighted in Figure 3.6c. Regions of the domain characterized by low cloud top heights (colder colors in Figure 3.6a) are generally identified as warm, single-layered clouds (both red and blue in Figure 3.6c). From Figure 3.6c, it is also clear that warm, single-layered grid boxes are generally more likely to be identified as non-raining (red) than raining (blue).

3.4 Interpreting path-integrated attenuation

In Section 2.3, it was noted that path-integrated attenuation due to hydrometeors (PIA) is used in conjunction with CPR reflectivity to determine rainfall incidence in the CloudSat precipitation retrieval algorithms. As PIA is, by definition, the integrated, two-way extinction of the radar signal due to interactions with hydrometeors, it was of interest to examine the relationship between PIA and more common and physical column-integrated quantities, such as cloud, drizzle and rain liquid water paths (CWP, DWP and RWP, respectively). To do so, water paths from the RAMS RCE simulation (Section 2.4) were compared directly to their corresponding QuickBeam-simulated 94-GHz PIA values (Section 3.3). From RAMS output, water path (WP) fields for the three liquid hydrometeor classes (cloud, drizzle and rain) were calculated using

$$WP = \sum_{i=1}^{N_{layers}} (r_i * \rho_{air,i}) \Delta z_i \quad ,$$

where N_{layers} is the number of model layers, r_i is the RAMS hydrometeor mixing ratio in a given model layer (kg kg^{-1}), $\rho_{air,I}$ is the air density in a given model layer (g m^{-3}), and Δz_i is

the model layer's depth (m). CWP, DWP and RWP were summed to give the total liquid water path (TWP) for each cloudy grid box. Mean RAMS CWP, DWP, RWP and TWP as functions of percentiles of QuickBeam PIA for the warm, single-layered cloud grid box subset are denoted by the respective blue, light green, dark green and black bold curves in Figure 3.7. For these modeled clouds, the mean relationship between PIA and TWP is approximately linear, indicating that PIA is a valid proxy for TWP. Moreover, CWP dominates both DWP and RWP in contributing to TWP for these modeled clouds. At PIA values below approximately 1 dB, TWP is comprised almost entirely of cloud water. Above this PIA value, the amount of precipitation water (drizzle and rain) contained within these modeled clouds increases with PIA.

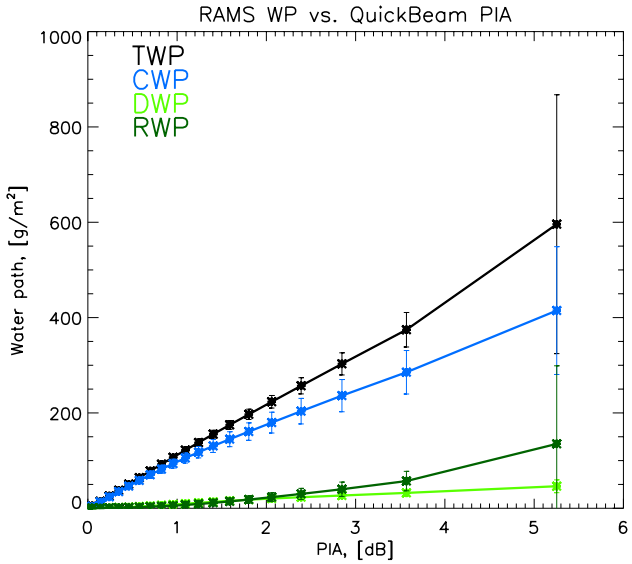

Figure 3.7. RAMS water path values as a function of percentiles of QuickBeam-simulated 94-GHz PIA for the warm, single-layered cloud grid box subset. Bold points represent the mean water path value in each PIA percentile bin. Bars represent the standard deviation about the mean. Total liquid water path (black) is the sum of cloud, drizzle and rain water paths (blue, light green and dark green, respectively).

Given these general relationships, PIA is interpreted as being representative of TWP in subsequent sections. It should be noted that by interpreting PIA in this manner, the

problem of cloud-rain water partitioning for a given PIA/TWP value is still quite relevant. In later sections, an analysis of rain occurrence as a function of PIA is used to provide insight into how cloud-rain water partitioning naturally occurs within warm clouds.

CHAPTER 4: OBSERVED AND MODELED WARM RAIN OCCURRENCE

4.1 Dependence upon path-integrated attenuation

One of the primary objectives of this study was to provide insight into the relationships between column-integrated water mass and the occurrence of warm rainfall. As was discussed in Section 1.2, methodologies designed to obtain estimates of cloud and precipitation properties from the total emission signal observed by passive microwave sensors must somehow partition this signal into cloud and rainwater components. A simple approach, first described by Wentz and Spencer (1998), solves this dilemma through application of a constant CWP partitioning threshold value of 180 g m^{-2}. Scenes in which the passive microwave estimate of TWP falls below this threshold are considered non-raining, and, as such, all water in the scene is understood to consist of cloud water. For scenes in which this threshold is surpassed, rain is assumed to be present, and the amount of cloud water in the scene is then related to the derived rain-column-averaged rain rate through an empirical relationship. The physical basis for this CWP threshold partitioning approach rests in a study of 38 northeast Pacific extratropical cyclones (Wentz 1990), wherein drizzle or light rain was determined to be likely when Special Sensor Microwave/Imager (SSM/I) retrievals of CWP surpassed 180 g m^{-2}. While the application of this fixed threshold value results in geographic rainfall distributions that are similar to those from other climatologies (Hilburn and Wentz 2008), this partitioning assumption may lead to errors in retrieved CWP – and, by association, RWP – that are on the order of tens of percent (O'Dell et al. 2008).

More recent studies have used data from multiple sensors in the A-Train to more directly explore the relationships between CWP and rain occurrence for liquid-phase clouds. Using rainfall incidence information from CloudSat pixels collocated with AMSR-E estimates of CWP derived from the aforementioned partitioning scheme of Wentz and Spencer (1998), Lebsock et al. (2008) noted that the probability of rainfall from warm, oceanic clouds increased as a monotonic function of CWP. Interestingly, at the 180 g m^{-2} partitioning threshold value, only 20-30% of the scenes were identified as raining, and non-negligible probabilities of rainfall were observed for CWP values below the threshold. Two subsequent studies followed a similar multi-sensor approach to further investigate these relationships. Figures 4.1a and 4.1b – from L'Ecuyer et al. (2009) and Suzuki et al. (2011), respectively – show the fractional occurrence of CloudSat-observed rainfall from warm, oceanic clouds as a function of collocated A-Train estimates of CWP. While the CWP values used in these studies are derived from different sensors and, as such, are based on different physical retrieval methodologies (L'Ecuyer et al. 2009: AMSR-E, microwave emission; Suzuki et al. 2011: MODIS, solar reflection), the similar resulting trends in these figures corroborate the monotonic relationship between warm rain occurrence and CWP noted by Lebsock et al. (2008). At the 180 g m^{-2} partitioning threshold, the percentage of CloudSat scenes that were flagged as raining certain was found to be relatively low (between 5 and 15%); moreover, non-negligible probabilities of non-raining scenes were found at high CWP values. These results suggest that rain onset does not occur at a specific CWP threshold; rather, rainfall becomes increasingly more likely as CWP increases.

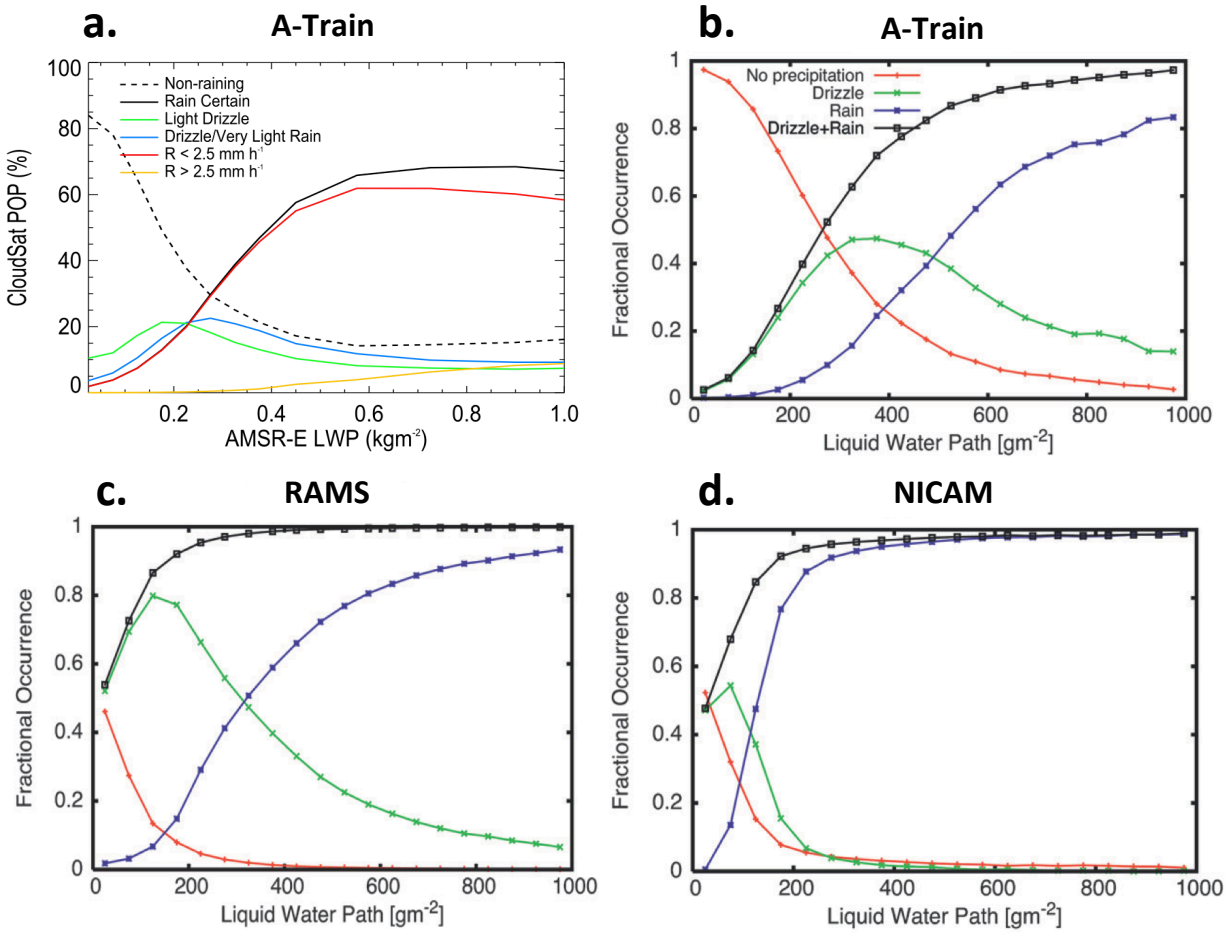

Figure 4.1. (a) Fractional occurrence of CloudSat-defined rainfall from oceanic warm clouds as a function of collocated (a) AMSR-E CWP (from L'Ecuyer et al. 2009) and (b) MODIS CWP (from Suzuki et al. 2011). (c) and (d) are as in (b), but for simulated oceanic warm clouds from (c) a large-domain RAMS RCE simulation and (d) a global simulation performed with the Non-hydrostatic Icosahedral Atmospheric Model (NICAM). For these latter two plots, the QuickBeam radar simulator was used to define rainfall in a manner consistent with the CloudSat results presented in (b). See Suzuki et al. (2011) for further details.

Suzuki et al. (2011) went on to explore the representation of these same relationships for warm, maritime clouds simulated with both RAMS and the Non-hydrostatic Icosahedral Atmospheric Model (NICAM). RAMS output from a large-domain, fine spatial-resolution, two-dimensional RCE simulation described by van den Heever et al. (2011) was analyzed alongside NICAM output from a global simulation described by Suzuki et al. (2008). While a single-moment microphysical scheme was employed within the

NICAM simulation, the RAMS simulation made use of the same two-moment bulk microphysical scheme used in the RAMS simulation analyzed within the present study. The QuickBeam radar simulator was applied to both NICAM and RAMS output to generate comparable, CloudSat-like warm rain statistics. Resulting fractional occurrences of drizzle (-15 dBZ $< Z_u <$ 0 dBZ; green) and rainfall ($Z_u >$ 0 dBZ; blue) as functions of CWP from RAMS and NICAM are shown in Figures 4.1c and 4.1d, respectively. While qualitatively consistent with the corresponding observationally-derived results in Figures 4.1a and 4.1b (i.e., the probability of modeled rainfall also increases monotonically with increasing CWP), drizzle and rain were generally more likely at any given CWP value within both RAMS and NICAM than was suggested by observations. For example, at a CWP value of 200 g m^{-2}, rain was approximately four times more likely within the RAMS simulation (~20%) than indicated by the CloudSat-MODIS data set (~5%). However, at this same CWP value, rain within NICAM was approximately sixteen times more likely (~80%) than observed. Based on these findings, the authors concluded that the conversion of cloud water to drizzle and rain water within both NICAM and RAMS occurred more quickly than is observed in reality.

The fact that RAMS warm rainfall statistics more closely mirrored observations than did those from NICAM was presumed by the authors to be largely attributable to cloud microphysical scheme differences between the two models. While the single-moment bulk microphysical scheme used within NICAM predicts only hydrometeor mixing ratios, the two-moment bulk microphysical scheme employed within the analyzed RAMS simulation predicts both hydrometeor mixing ratios and number concentration, and, thus, acts to better characterize the hydrometeor distributions. The resulting representation of warm

rain processes within RAMS results in a more realistic evolution of the droplet size spectra from cloud to rain (Meyers et al. 1997).

In this study, PIA is used as a proxy for column-integrated liquid water mass to explore similar statistics of warm rain occurrence within the CloudSat and RAMS data sets. Given the direct relationships between PIA and both CWP that were explored in Section 3.4 and the previously described links between CWP and warm rain likelihood, the hypothesis for this section of the study was that warm rain occurrence should also increase with PIA. It is noted here that while PIA is more directly representative of TWP (Figure 3.7), TWP is predominantly comprised of cloud water at low TWP values (Lebsock et al. 2011), and, thus, PIA should also serve as an adequate proxy for CWP at low TWPs. Figure 4.2 shows the ratio of raining counts to total (raining and non-raining) counts as a function of percentiles of PIA for the CloudSat warm, single-layered cloud data set. In line with the stated hypothesis, rain likelihood increases as a monotonic function of increasing PIA. While observed rain is all but certain at PIA values approaching 12 dB, the wide spacing of percentile bins (nodes in Figure 4.2) at high PIA values indicates that encountering warm clouds with these characteristics is relatively unlikely; warm clouds more commonly have low PIA values and are more likely to be flagged as non-raining. Warm rain is more likely than not (fractional occurrence of 50%; green dotted line in Figure 4.2) at a PIA value of approximately 3 dB, which according to the RAMS-derived relationships in Figure 3.7, corresponds to a CWP value of 250 g m^{-2}.

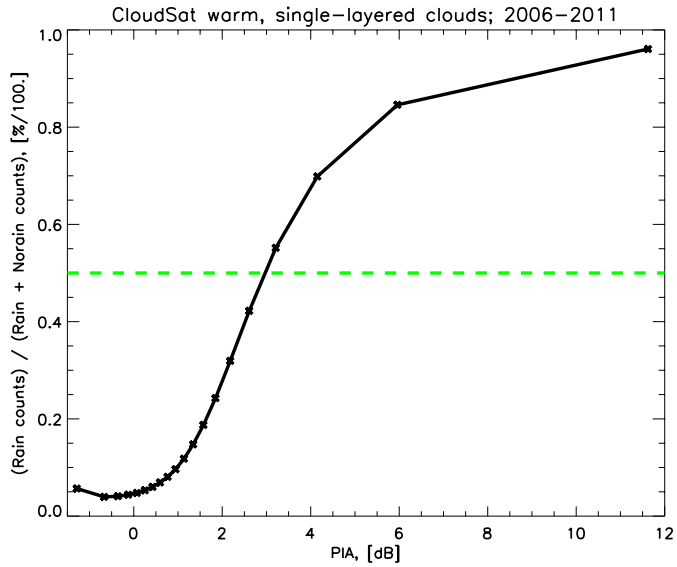

Figure 4.2. Fraction of raining to total CloudSat scenes as a function of percentiles of 2C-PRECIP-COLUMN path-integrated attenuation (PIA) for the warm, single-layered cloud subset. Nodes represent the median PIA within each PIA percentile bin. In this and subsequent similar figures, the dotted green line is plotted at a constant fractional occurrence of 50% to indicate where rain is more likely than not.

The corresponding relationships between rain occurrence and column-integrated quantities for the RAMS warm, single-layered cloud subset are shown in Figure 4.3. Immediately evident is the familiar monotonic increase in rain likelihood with increasing QuickBeam-derived PIA (Figure 4.3a). However, in comparison to the CloudSat trend in Figure 4.2, a similar magnitude increase in rain occurrence occurs over a smaller PIA range within the RAMS data set. Over the PIA interval spanning 1 to 3.5 dB, RAMS rain likelihood increases from approximately 5 to 95%; within the CloudSat data set, rain likelihood increases from approximately 5 to 60% over the same PIA interval. Moreover, rain within RAMS is more likely than not at a PIA value of 2 dB, approximately 1 dB lower than is observed by CloudSat. In short, RAMS-simulated clouds rain more frequently at lower PIA values than they do in nature, in line with the findings of Suzuki et al. (2011) and again

suggesting that the conversion of cloud to rainwater occurs more quickly within RAMS than is observed.

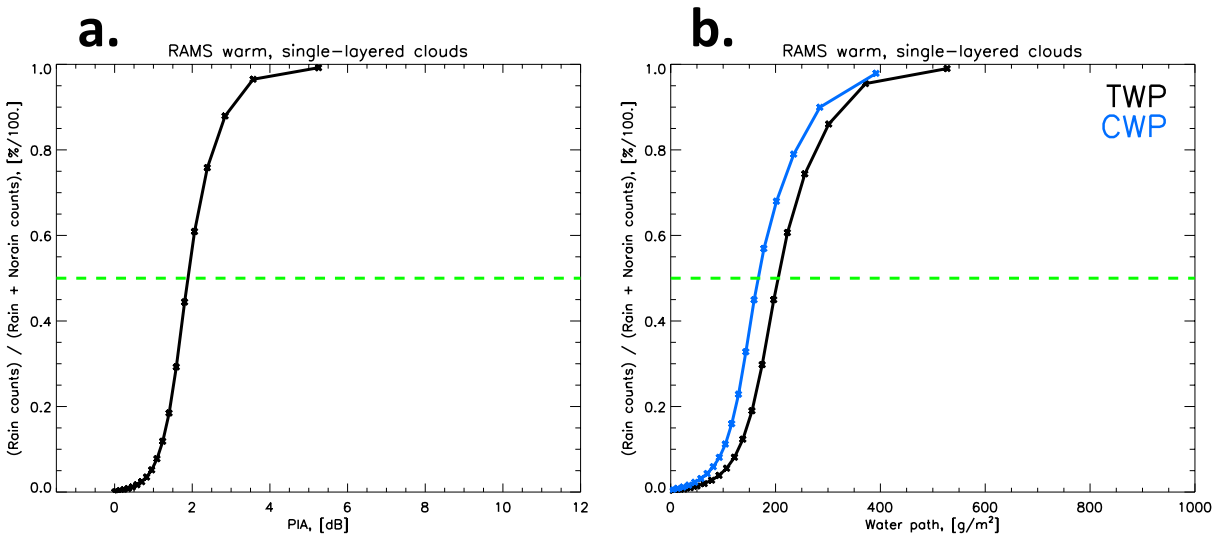

Figure 4.3. Fractional occurrence of RAMS rainfall as a function of percentiles of (a) QuickBeam-derived PIA and (b) cloud (blue) and total (black) liquid water paths for the warm, single-layered cloud subset. Nodes represent the median x-axis value in each x-axis percentile bin.

The percentile portion of this analysis reveals that the CloudSat distribution of PIA for these warm clouds (Figure 4.2) extends to higher values than are simulated with RAMS (Figure 4.3a). The median PIA value of the 95th – 100th CloudSat PIA percentile bin is twice as large as that from RAMS (~ 11.5 and 5.5 dB, respectively). If rain removes water mass from the atmospheric column, rainfall would act to limit the maximum attainable PIA within the warm cloud distributions. As RAMS clouds are more likely to rain at low PIA values, this may suggest that RAMS clouds are more likely to rain out their water mass before attaining the higher PIA values observed in the CloudSat distribution. This implies that more water mass may build up within real clouds before it is rained out.

For direct comparison with the results from Suzuki et al. (2011), RAMS rainfall occurrence is also plotted as a function of CWP in Figure 4.3b (blue curve). Echoing the PIA results and in keeping with the findings of Suzuki et al. (2011), rain within RAMS is generally more likely at all CWP values than is observed (Figures 4.1a and 4.1b), again suggesting that the conversion of cloud water to rain water within RAMS occurs more quickly than in nature. However, these differences may be even more pronounced in the present study than is suggested by Suzuki et al. (2011). Whereas the latter study showed that rain within RAMS did not exceed a fractional occurrence of 50% until CWP surpassed 300 g m^{-2} (Figure 4.1c), the same point is eclipsed at an approximate CWP of 150 g m^{-2} within the present analysis. It is worth noting that both RAMS RCE simulations were initialized from tropical soundings and were characterized by a 300 K underlying SST, and Suzuki et al. (2011) employed the same rain definition (QuickBeam-derived $Z_u > 0$ dBZ) as is used within the present study (Table 2.1). However, Suzuki et al. (2011) utilized RAMS output from all of the aerosol concentration sensitivity experiments described by van den Heever et al. (2011). In those experiments, aerosol concentrations between 2 and 4 km were varied from 25 to 1600 cm^{-3}, spanning a much greater range than the height-invariant 100 cm^{-3} concentrations characterizing the RAMS simulation analyzed within the present analysis. It is therefore plausible that the inclusion of the higher aerosol concentration experiments within the warm rain statistics reported by Suzuki et al. (2011) effectively acted to shift the warm rain occurrence trends towards higher CWPs, in line with the proposed second aerosol indirect effect (Albrecht 1989).

Not discussed thus far is how the cloud life cycle may be intertwined with these results. As both observational and model statistics presented within this section are

obtained from many "snapshot" (i.e., static) scenes, assuming the full cloud life cycle is adequately captured within both data sets, they are inherently representative of composite characteristics from clouds that are in various stages of development, maturity or decay. No attempt has yet been made to isolate any single stage of the full cloud life cycle. However, we argue here that column-integrated quantities such as CWP and PIA are related to different portions of the cloud life cycle. For example, in a study of trade wind cumulus clouds modeled within a three-dimensional LES framework, Witte et al. (2013) noted that cloud volume (depth) – and, by association, CWP – increased as the clouds developed to their mature stage. Once this mature stage was reached, however, active precipitation fall out and entrainment functioned to deplete liquid water within the clouds, causing cloud depth and CWP to decrease back to values observed during the development stages. Thus, while PIA and CWP may be imperfect, non-monotonic sole metrics from which to diagnose relative cloud maturity, it was shown within this section that clouds with higher PIA and CWP attributes are more likely to be actively raining. This may suggest that clouds with these column-integrated characteristics are, indeed, nearing the more mature stages of their life cycle. Whether any differences that may exist in modeled and observed warm cloud life cycle help to explain the differences between RAMS-simulated and CloudSat-observed relationships between column-integrated water mass and rainfall occurrence is a topic explored in Section 4.4.

4.2 Relationship with cloud geometric properties

In this section, the relationships between warm rainfall occurrence and cloud depth, another cloud macrophysical property, are explored. Such an analysis is not without

precedent. Indeed, attempts to characterize these very relationships using direct observations have been a subject of study for decades. Byers and Hall (1955) used observations from two aircraft to determine what percentage of warm, over-ocean trade wind cumulus clouds in the vicinity of Puerto Rico contained rain hydrometeors as a function of cloud top height. While one aircraft would penetrate randomly selected clouds and use a nose-mounted 3-cm radar to search for rain echoes (drop diameters ≥ ~ 150 μm), the other would fly in formation at cloud-top level, recording altitude. Using these data, the authors determined that the likelihood of warm, oceanic clouds containing rain hydrometeors within their volume increased markedly with increasing cloud top height (Figure 4.4a). While clouds with tops below 6000 ft (~1800 m) were not likely to contain a rain echo, those with tops exceeding 11500 ft (~3500 m) were all but certain to contain such an echo. Relevant to the initiatives of the present study, the authors suggested that because cloud base heights were relatively uniform over the ocean surface, cloud top height could be used as a proxy for cloud depth. However, it is important to note that merely requiring that clouds contain rain echoes within their volume does not necessarily guarantee that that rain is reaching either cloud base or the surface.

With the recent advent of space-borne profiling radars has come the ability to analyze these same relationships on both greater spatial scales and longer temporal scales. CloudSat, in particular, has proven a useful tool to this end. In summarizing early CloudSat mission performance, Stephens et al. (2008) made use of CloudSat rainfall incidence estimates from the 2C-PRECIP-COLUMN product (Haynes et al. 2009) in conjunction with cloud depth estimates from the 2B-GEOPROF product (Marchand et al. 2008) to study rainfall characteristics for warm clouds over the global oceans. The authors showed that

the probability of rainfall increases with increasing cloud depth (Figure 4.4b, blue curve). While warm clouds with depths below 0.5 km were almost never flagged as certainly raining, those with depths greater than 2.5 km were observed to rain ~55% of the time. While qualitatively consistent with the early results from Byers and Hall (1955), these CloudSat results indicated that rainfall from deeper warm clouds was not as ubiquitous as was suggested by the former study. However, in contrast to the methodology of Byers and Hall (1955), the rainfall incidence information derived from the CloudSat 2C-PRECIP-COLUMN precipitation flag is physically indicative of the presence of rain adjacent to, if not reaching, the ocean surface (i.e., not just located somewhere within the cloud volume). Therefore, when taken together, the results from these two studies may suggest that while deeper warm clouds are likely to produce rain hydrometeors somewhere within their volume, this rain does not always actively fall from cloud base.

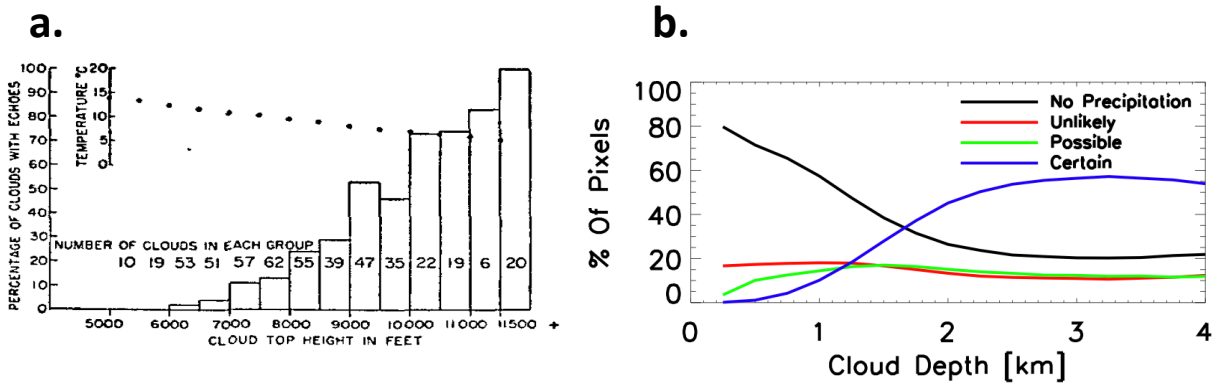

Figure 4.4. (a) The percentage of warm, maritime cumulus clouds that contained a precipitation radar echo as a function of cloud top height. From Byers and Hall (1955). (b) The percentage of CloudSat-identified warm, maritime clouds that were flagged as certainly raining (blue) and non-raining (black) as a function of cloud depth. From Stephens et al. (2008).

It was of interest to both validate these previous observationally-derived links between cloud geometric properties and warm rain occurrence through the use of a longer

CloudSat data record and to compare them with those derived from warm clouds simulated with RAMS. In order to ensure that observed and simulated warm clouds were rooted within the boundary layer (i.e., *not* high-based fragments of cloud situated below the freezing level), the analysis was further restricted to raining and non-raining warm, single-layered clouds with equal cloud echo base heights. The mean cloud echo base height for the CloudSat warm, single layered cloud distribution was approximately 770 m, with little latitudinal variation (Figure 3.2a). Thus, cloud echo base height for the CloudSat distribution was fixed around 720 m, the nominal height of the nearest CloudSat vertical range gate. For consistency, the RAMS warm cloud distribution was restricted to those with echo bases at 770 m, the nearest vertical model level height. This screening step reduced the total number of CloudSat and RAMS clouds analyzed to 3.2 and 70.2 million, respectively. However, despite these data volume reductions, the relative proportion of observed and simulated raining clouds before and after this additional screening step remained largely consistent. While the percentage of CloudSat raining clouds decreased from 25.4% to 22.3% by constraining cloud echo base height, the percentage of RAMS raining clouds increased slightly from 27.4 %to 27.9% through application of the same constraint.

The composite relationship between warm rain occurrence and percentiles of cloud depth (variable cloud echo top height above a fixed cloud echo base height) for the remaining CloudSat-observed warm cloud distribution is shown in Figure 4.5a. Qualitatively consistent with aforementioned results from Byers and Hall (1955) and Stephens et al. (2008), rainfall is increasingly more likely as warm clouds become deeper. While the shallowest clouds in the distribution (~0.5 km deep) rain with a relative

frequency of 10%, the deepest clouds in the distribution (~3.0 km deep) are flagged as raining approximately 40% of the time. The deepest warm clouds analyzed in this study were found to produce rainfall slightly less often than was reported by Stephens et al. (2008) (Figure 4.4b). As the rainfall occurrence trend in Figure 4.5 did not change appreciably when the analysis was restricted to the early (2006 – 2007) CloudSat observations summarized by Stephens et al. (2008), these differences are likely related to the present study's use of a fixed cloud echo base height requirement.

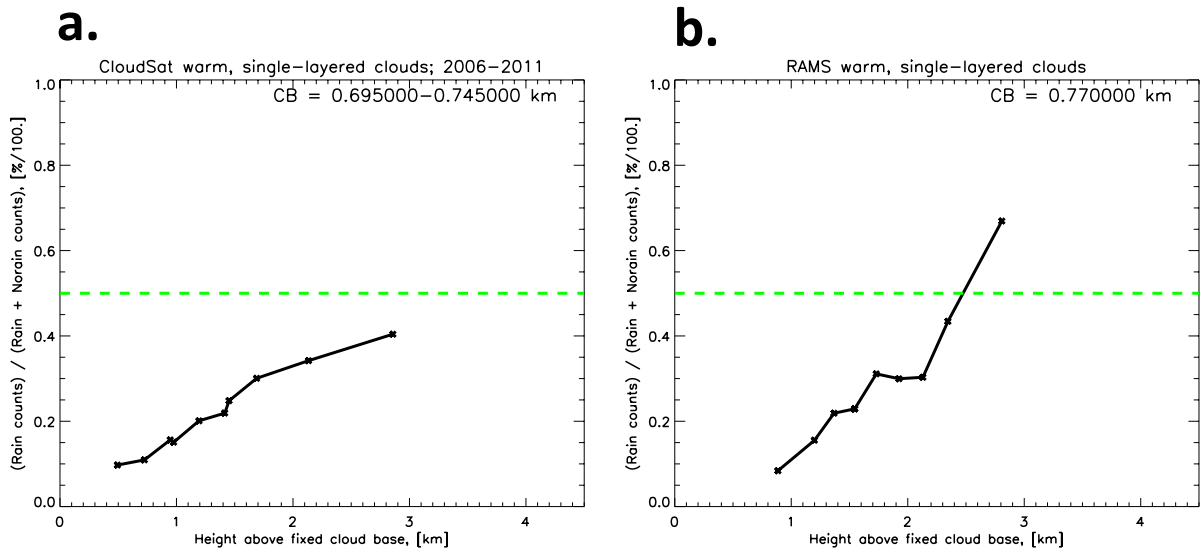

Figure 4.5. Fractional occurrence of rainfall as a function of percentiles of cloud depth (cloud top height above a fixed cloud base height) for the (a) CloudSat and (b) RAMS warm, single-layered cloud data sets. Nodes represent the median cloud depth in each cloud depth percentile bin.

The corresponding composite relationship between rainfall occurrence and cloud depth for warm clouds simulated with RAMS is shown in Figure 4.5b. Similar to the CloudSat-derived trends, simulated warm rain also becomes more likely as cloud depth increases. However, the CloudSat and RAMS relationships are quantitatively less consistent. Namely, while the frequency of occurrence of rainfall for the shallowest observed and simulated clouds (depths below ~2.5 km) are remarkably comparable, the

deepest warm clouds within RAMS rain increasingly more often than is suggested by the CloudSat observations. As cloud depths approach 3 km, RAMS warm clouds rain approximately 30% more often than do those identified by CloudSat. The percentiles of the CloudSat and RAMS cloud depth distributions (nodes in Figure 4.5) are very comparable, indicating that these differences are robust.

These results motivated two simple questions: 1) Why are deeper observed and simulated warm clouds more likely to rain?; and 2) Why do the deepest simulated warm clouds rain more often than they do within nature? In Section 4.1, it was shown that CloudSat-observed and RAMS-simulated warm clouds were also more likely to rain as column-integrated water mass increased. However, column-integrated water mass is directly related to cloud depth. Indeed, in adiabatic conceptualizations of clouds, wherein cloud liquid water content increases linearly with height above cloud base, adiabatic CWP is proportional to the square of cloud depth (Albrecht et al. 1990; Pawlowska and Brenguier 2003). Less theoretically, Kubar et al. (2009) noted that the spatial variation of mean CWP for warm oceanic clouds identified by joint CloudSat-MODIS observations closely mirrored that of the mean cloud-top height field; areas characterized by higher mean cloud-top heights were also those where mean CWP was high, and vice versa. The authors argued that given cloud base heights are relatively constant over the ocean surface, cloud-top height acted as an adequate proxy for cloud depth and, thus, the spatial similarity of the two fields implied that deeper clouds contained more column-integrated liquid water.

In light of these loose relationships between column-integrated liquid water mass and cloud depth and in an attempt to answer the two simple questions put forth in the

previous paragraph, the relationships between PIA and cloud depth were explored for the warm, single-layered clouds within the CloudSat and RAMS data sets. Figures 4.6a and 4.6b show the mean (bold) PIA as a function of percentiles of cloud depth for all (raining and non-raining; black) CloudSat-observed and RAMS-simulated warm clouds, respectively. In general, PIA increases with increasing cloud depth for all clouds in both data sets. In the mean, deeper warm clouds contain more and/or larger liquid hydrometeors that act to collectively attenuate the real and simulated 94-GHz radar beam to a greater degree. Thus, deeper warm clouds – those which have been shown to rain more often than their shallower counterparts – are associated with higher PIA, a cloud macrophysical characteristic that was also linked to higher probabilities of rainfall (Figures 4.2 and 4.3a). Physically, these results collectively imply that it is the increased availability of liquid water within deeper clouds that preferentially promotes the production of rainfall through warm rain processes within these clouds, consistent with the conclusions of Reiche and Lasher-Trapp (2010).

While qualitatively similar to the observed cloud depth-PIA relationships in Figure 4.6a, the RAMS trends in Figure 4.6b exhibit notable quantitative differences that provide insight into the warmfall rain occurrence discrepancies in Figure 4.5. First, it is interesting to note that for similar shallow warm cloud depths, the mean QuickBeam-derived RAMS PIA values are actually slightly lower than the mean of those observed by CloudSat. For cloud depths less than 2.5 km, RAMS PIA values are on average approximately 0.3 dB lower than observed. While this tendency would otherwise result in lower fractional occurrences of rainfall from RAMS-simulated shallow warm clouds, RAMS clouds produce rainfall more often at lower PIA values than is observed by CloudSat, a point that suggests the conversion

of cloud to rainwater occurs more quickly within RAMS than in nature (Section 4.1). These factors act to negate one another, resulting in similar rainfall probabilities from observed and simulated warm clouds with depths less than ~2.5 km (Figure 4.5). At cloud depths approaching 3 km, RAMS-simulated warm clouds have higher PIA values than are observed. For example, the mean QuickBeam-derived RAMS PIA at a cloud depth of ~2.8 km exceeds that observed by CloudSat by approximately 0.7 dB. Coupled with the finding that rainfall within RAMS is more likely at any given PIA value than CloudSat observations indicate, this result may again highlight that the conversion of cloud to rain water occurs more quickly than is observed within nature.

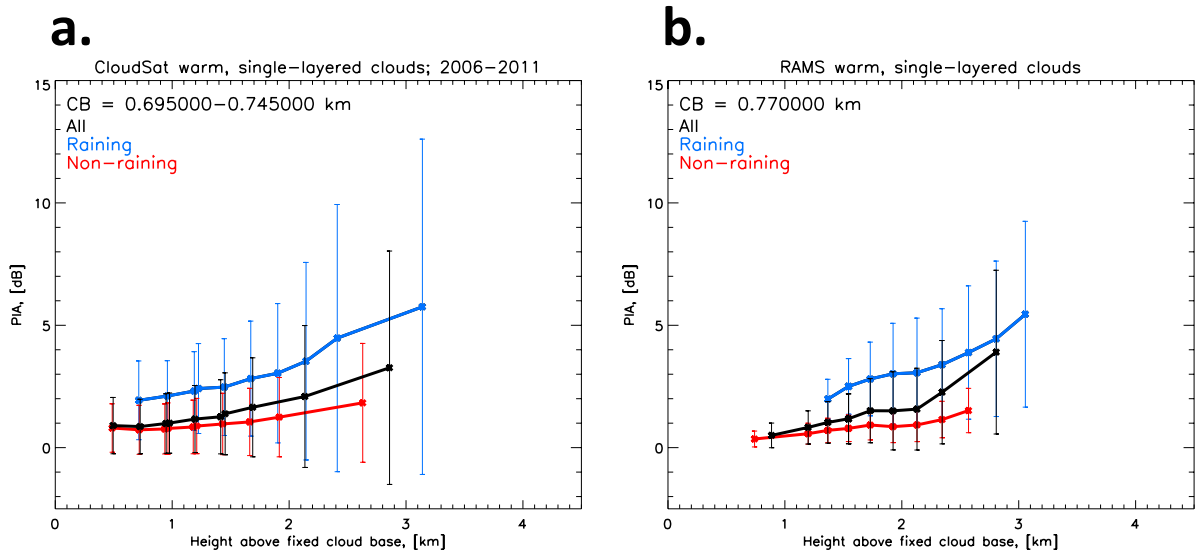

Figure 4.6. Mean PIA as a function of percentiles of cloud depth (cloud echo top height above a fixed cloud echo base height) for the (a) CloudSat and (b) RAMS warm, single-layered cloud subsets. Bold points represent the mean PIA values for a given cloud depth percentile bin. Bars represent the standard deviation of PIA about the mean.

Other plausible reasons for why warm rainfall occurrence increases with cloud depth may simply be related to time. Developing warm clouds inherently require some amount of time to grow to progressively deeper depths. If more integrated time is necessary for deeper warm clouds to achieve their greater altitudes, the amount of time

available for warm rain processes to act within these clouds would also be increased, a factor which is more conducive to the production of rainfall (e.g., Reiche and Lasher-Trapp 2010). In an observational case study, Burnet and Brenguier (2010) used radar data to track the evolution of three warm, shallow cumulus clouds that developed within the same immediate environment near the east central coast of Florida. While the tops of the first two clouds ascended from 2 to 3 km over the course of 8.5–10 minutes before collapsing without producing any rain, the third cloud ascended from a cloud-top height of 2 to 4 km over a span of approximately 15 minutes, producing appreciable rainfall. That is, the cloud that achieved the greatest depth over a the longest time interval was the only one which produced precipitation, anecdotally highlighting the relationship between cloud depth and time and underscoring how these factors may be mutually related to the production of rainfall. As was the case for the PIA-rainfall relationships highlighted in Section 4.2, the composite relationships between cloud depth and rainfall derived within this section are inherently representative of clouds in various stages of development, maturity and decay. As they are produced from averaging many "snapshot" scenes, it is not known, for instance, what percentage of 2-km deep clouds ascended to greater depths or produced rainfall at later times. The relationships between cloud life cycle, cloud macrophysical characteristics and rainfall are explored in further detail within Section 4.4.

4.3 Relationship with cloud layer attenuation

Thus far, it has been shown that the likelihood of warm rain from CloudSat-observed and RAMS-simulated liquid-phase clouds increases with both increasing PIA (Section 4.1) and increasing cloud depth (Section 4.2). However, these two cloud

macrophysical characteristics are, in some ways, related to one another (Figure 4.6). As cloud depth increases, mean PIA also increases, implying that deeper clouds contain more and/or larger liquid hydrometeors that collectively act to attenuate a 94-GHz radar beam to a greater degree. This result is somewhat unsatisfying; if cloud depth and PIA are, in the mean sense, directly related to one another and increasing values of each factor are associated with progressively higher probabilities of rainfall, it is not clear which of these two cloud macrophysical characteristics is *more* strongly associated with the production of rainfall from warm clouds. The aim of this section is to clarify some of this ambiguity by investigating the joint probability that warm clouds with given pairs of PIA and depth attributes produce rainfall. In doing so, insight is gained into how the concentration of liquid water within these observed and simulated warm clouds influences their propensity to precipitate.

The methodology developed to investigate these joint probabilities of rainfall relies upon sequential percentile partitions of the warm cloud data sets with respect to PIA and cloud depth. First, decile values of PIA are identified for the CloudSat and RAMS warm, single-layered cloud distributions that remained after applying a fixed cloud echo base height requirement (Table 4.1). By using these resulting PIA decile values to define bin boundaries, this step ensured that approximately equal numbers of warm cloud counts existed within each PIA bin. The overarching goal of this initial division was to fix PIA within each bin; that is, in order to adequately separate the influences of PIA and cloud depth on the warm rain occurrence statistics, it was desirable for the width of the PIA percentile bins to be as small as possible. The CloudSat and RAMS PIA percentile bin values summarized in Table 4.1 indicate that the width of most bins is less than 1 dB. To ensure

that the warm rain statistics were not skewed by outlier PIA values in the high- and low-end tail bins, the analysis was restricted to observed and simulated PIA values that fell between the respective 10th and 90th percentile values (i.e., the eight middle PIA decile bins). Within each of the remaining PIA percentile bins, decile values of cloud depth were calculated and used to define corresponding bin boundaries. With these two percentile partitioning steps complete, each PIA-cloud depth percentile bin pair within the CloudSat and RAMS data sets contained approximately 32,100 and 702,200 warm cloud scenes, respectively.

Table 4.1. PIA percentile bin values and related statistics for CloudSat (top) and RAMS (bottom) warm, single-layered clouds with fixed cloud echo base heights.

Data set	Percentile bin	PIA bin minimum, [dB]	PIA bin maximum, [dB]	PIA bin width, [dB]	Bin median PIA, [dB]
CloudSat	0th - 10th	-127.44	-0.35	127.10	-0.71
	10th - 20th	-0.35	0.10	0.45	-0.10
	20th - 30th	0.10	0.45	0.34	0.28
	30th - 40th	0.45	0.76	0.31	0.60
	40th - 50th	0.76	1.07	0.32	0.91
	50th - 60th	1.07	1.42	0.35	1.24
	60th - 70th	1.42	1.85	0.43	1.62
	70th - 80th	1.85	2.45	0.60	2.12
	80th - 90th	2.45	3.53	1.08	2.88
	90th - 100th	3.53	54.75	51.22	4.74
RAMS	0th - 10th	0.00	0.10	0.10	0.02
	10th - 20th	0.10	0.31	0.21	0.21
	20th - 30th	0.31	0.54	0.23	0.43
	30th - 40th	0.54	0.79	0.24	0.66
	40th - 50th	0.79	1.05	0.26	0.91
	50th - 60th	1.05	1.34	0.30	1.19
	60th - 70th	1.34	1.72	0.37	1.52
	70th - 80th	1.72	2.24	0.52	1.95
	80th - 90th	2.24	3.18	0.95	2.62
	90th - 100th	3.18	75.74	72.56	4.19

The execution of these two distinct partitioning steps acts to stratify the observed and simulated warm cloud distributions in physically meaningful ways. Mean values of

RAMS in-cloud averaged total water content (the sum of cloud, drizzle and rain water contents; TWC) as a function of percentiles of cloud depth within each PIA percentile bin (colored curves) are shown in Figure 4.7. When PIA is fixed along any given colored curve, the mean in-cloud averaged TWC decreases with increasing cloud depth. That is, deeper warm clouds with roughly the same amount of column-integrated total water mass as shallower clouds are, in a sense, less "dense," or contain lower average concentrations of liquid water within their increased volumes. For any given cloud depth, the mean in-cloud averaged TWC increases with increasing PIA, indicating that clouds with the same depth but increasing amounts of total column-integrated water mass intuitively contain higher average concentrations of liquid water within their volumes. As estimating the vertical distribution of water mass within a given CloudSat profile would inherently require additional assumptions about the observed hydrometeor distributions, no attempt is made to compute in-cloud averaged TWC for the warm clouds identified by CloudSat. However, it is expected that the RAMS-derived trends in Figure 4.7 should hold – at least in a qualitative sense – for the CloudSat warm cloud distribution.

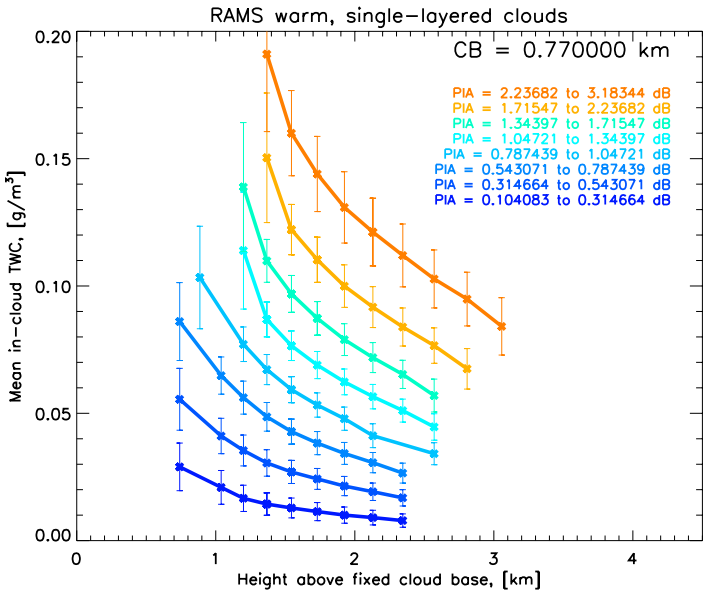

Figure 4.7. Mean in-cloud total water content (TWC) as a function of percentiles of cloud depth, stratified by percentiles of PIA (colored curves) for RAMS warm, single-layered clouds. Nodes along each PIA curve represent the median cloud depth values within each cloud depth percentile bin. Bars indicate the standard deviation of in-cloud averaged TWC about the mean value in each PIA-cloud depth bin.

While these stratifications act to fix the total number of warm, cloudy scenes within each PIA-cloud depth percentile bin pair, the relative proportions of raining and non-raining scenes within each stratified distribution remain variable. To assess the relative likelihood of rainfall as a simultaneous function of both PIA and cloud depth, the fraction of raining-to-total counts within each paired bin was calculated. The resulting fractional occurrences of warm rainfall as a function of cloud depth, stratified by PIA are shown in Figure 4.8. Beginning with the RAMS trends in Figure 4.8b, for any given fixed cloud depth, simulated warm rainfall becomes increasingly more likely with increasing PIA. As PIA increases for warm clouds of the same depth, the mean in-cloud averaged TWC also increases (Figure 4.7), amplifying the amount of liquid water available for warm rain processes represented within the model and supporting more probable rainfall production. Along any given fixed PIA curve, RAMS warm rainfall generally becomes less likely – or, in

the case of the lowest PIA percentile bins, remains equally unlikely – as cloud depth increases. Intuitively, warm rainfall is less likely when the same amount of water is spread over a deeper cloud layer, as this scenario results in lower mean in-cloud averaged TWC. These trends collectively underscore the importance of liquid water availability for the production of warm rainfall within RAMS.

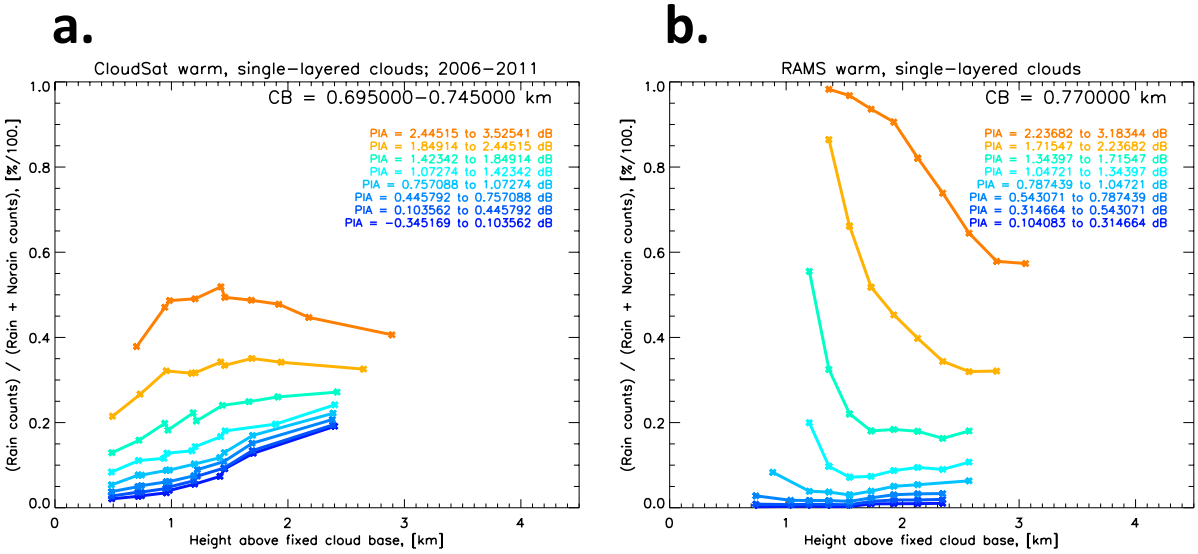

Figure 4.8. Fractional occurrence of rainfall as a function of percentiles of cloud depth, stratified by percentiles of PIA (colored curves) for warm, single-layered clouds (a) observed by CloudSat and (b) simulated with RAMS. Nodes along each PIA curve represent the median cloud depth values within each cloud depth percentile bin.

Despite comparable CloudSat and RAMS PIA percentile bins (Table 4.1) and correspondingly similar cloud depth distributions, the fractional occurrences of warm rainfall derived from the CloudSat warm cloud data set (Figure 4.8a) are, at first glance, drastically different from those characterizing the RAMS data set. While observed warm rain from clouds of the same depth is also increasingly more likely with increasing PIA, the magnitude of this increase is less pronounced than is suggested by the RAMS trends (Figure 4.8b). For the highest comparable PIA values, observed warm rainfall at any cloud

depth is less likely than is simulated with RAMS. These quantitative differences are reminiscent of, and related to, the differences between the observed and simulated PIA-warm rain occurrence trends discussed in Section 4.1. As was noted in the latter section, in comparison to rainfall from warm clouds observed by CloudSat, the likelihood of rain from RAMS-simulated warm clouds increases more sharply as a function of increasing PIA, a result that suggests simulated warm rain processes too quickly convert cloud water to rain.

When observed and simulated PIA are fixed about similar values, the variation of CloudSat warm rainfall likelihood with respect to cloud depth is markedly different than that from RAMS. Along most of the lower CloudSat PIA percentile bin curves in Figure 4.8a, the fractional occurrence of rainfall actually increases with increasing warm cloud depth, in direct opposition to the RAMS-derived relationships in Figure 4.8b. This trend is most pronounced for the lowest CloudSat PIA percentile bins; for warm clouds with PIA values between ~ 0.1 and 0.4 dB (second darkest blue curve), the observed likelihood of rainfall increases from ~ 5% to 15% as cloud depth increases from 1 to 2 km. This would imply that deeper observed warm clouds with the same PIA as their shallower counterparts are actually more likely to rain, despite having lower average concentrations of liquid water mass within their volumes. While the likelihood of RAMS-simulated warm rainfall is strongly governed by the availability of water within a cloud, such a relationship is not as clearly defined for clouds observed within nature. In contrast to these low PIA trends, CloudSat-observed rainfall likelihood as a function of cloud depth within the highest PIA percentile bin is more similar to that from RAMS. For CloudSat-observed warm clouds with PIA values between ~ 2.5 and 3.5 dB (darkest orange curve in Figure 4.8a), rainfall generally becomes less likely as cloud depth increases from ~ 1.25 to 3 km.

The CloudSat-derived results presented within this section are largely counterintuitive. One might expect the relative likelihood of rainfall with respect to PIA and cloud depth to be largely dependent upon the availability of water within a cloud, as it is within RAMS data set. Hence, the rest of this thesis is devoted to better understanding the intervening factor or factors responsible for determining whether or not an observed warm cloud with relatively little column-integrated liquid water mass will produce rainfall.

4.3.1 Additional observational stratifications

By directly comparing the statistical relationships between warm rainfall occurrence and cloud macrophysical properties from CloudSat and RAMS, it has been inherently assumed that the modeled and observed warm cloud distributions are comparable in the first place. That is, the analysis thus far has assumed that actual warm clouds observed through the lens of CloudSat on a near-global scale are directly comparable to those simulated within a model domain characteristic of a tropical environment. The validity of such an assumption is tested within this subsection. To ensure that the CloudSat-RAMS differences discussed in Section 4.3 are not related to either physical differences between the two warm cloud distributions or the nature of the warm cloud observations themselves, the CloudSat warm, single-layered cloud distribution is further constrained through a series of experiments designed to facilitate more direct comparisons of observed and simulated rainfall statistics. These additional CloudSat constraints, and basic characteristics of the resulting raining and non-raining warm cloud distributions, are summarized in Table 4.2. The relative influence of each of these factors

on the CloudSat-RAMS rainfall occurrence differences outlined within Section 4.3 are discussed throughout the rest of this subsection.

Table 4.2. List of additional CloudSat warm, single-layered cloud stratification experiments and associated resulting raining and non-raining cloud distribution metrics. For the seasonal tests, NH and SH denote the Northern and Southern Hemispheres, respectively.

Additional Stratification	Non-raining warm cloud counts	Raining warm cloud counts	Fraction of raining to total cloud counts, [%]
None (reference)	2.50×10^6	7.15×10^5	22.26
DJF: NH (SH)	1.63×10^5 (3.16×10^5)	5.00×10^4 (8.19×10^4)	23.52 (20.56)
MAM: NH (SH)	1.44×10^5 (3.57×10^5)	4.09×10^4 (9.91×10^4)	22.17 (21.70)
JJA: NH (SH)	1.73×10^5 (3.48×10^5)	5.71×10^4 (1.12×10^5)	24.85 (24.39)
SON: NH (SH)	1.87×10^5 (4.25×10^5)	5.89×10^4 (1.03×10^5)	23.92 (19.48)
SST = [299.75, 300.25] K	9.91×10^4	3.52×10^4	26.19
Tropics (20°N - 20°S)	1.05×10^6	3.39×10^5	24.35
Low LTSS	4.17×10^5	1.49×10^5	26.27
High LTSS	4.75×10^5	9.02×10^4	15.95
Ascending orbit portions	8.29×10^5	2.47×10^5	22.95
Descening orbit portions	1.36×10^6	3.87×10^5	22.12

To assess the stability of the CloudSat-derived relationships in Figure 4.8a, the CloudSat warm, single-layered cloud distribution was first stratified by season. Within each hemisphere, CloudSat-observed warm clouds were aggregated over: December, January, and February (DJF); March, April, and May (MAM); June, July, and August (JJA); and September, October, and November (SON). While there is some subtle seasonal variation evident in the overall fraction of raining warm clouds identified within the resulting distributions (Table 4.2, last column), warm rainfall frequency within each hemisphere and throughout each season is largely comparable to that from the full warm cloud data set (Table 4.2, first row). Figure 4.9 shows the fractional occurrence of rainfall as a function of percentiles cloud depth, stratified by percentiles of PIA for each season within the Northern Hemisphere. Despite smaller sample sizes and some associated noise, these trends are, in general, very comparable to those characterizing all seasons within both hemispheres

(Figure 4.8a). For a given cloud depth, warm rainfall within each season is again increasingly more likely with increasing PIA. Moreover, within a given low PIA percentile bin, the puzzling increase in rainfall occurrence with cloud depth is still evident within each season. The corresponding seasonal rainfall occurrence trends from the Southern Hemisphere are highly comparable to the boreal relationships shown in Figure 4.9, and are therefore not shown. In short, the relationships between cloud macrophysical characteristics and warm rain occurrence within any one season does not come closer to resembling the RAMS-derived trends in Figure 4.8b. Furthermore, the collective lack of a strong seasonal signal within these CloudSat-derived warm rainfall occurrence trends implies that the corresponding CloudSat relationships in Figure 4.8a are indeed robust.

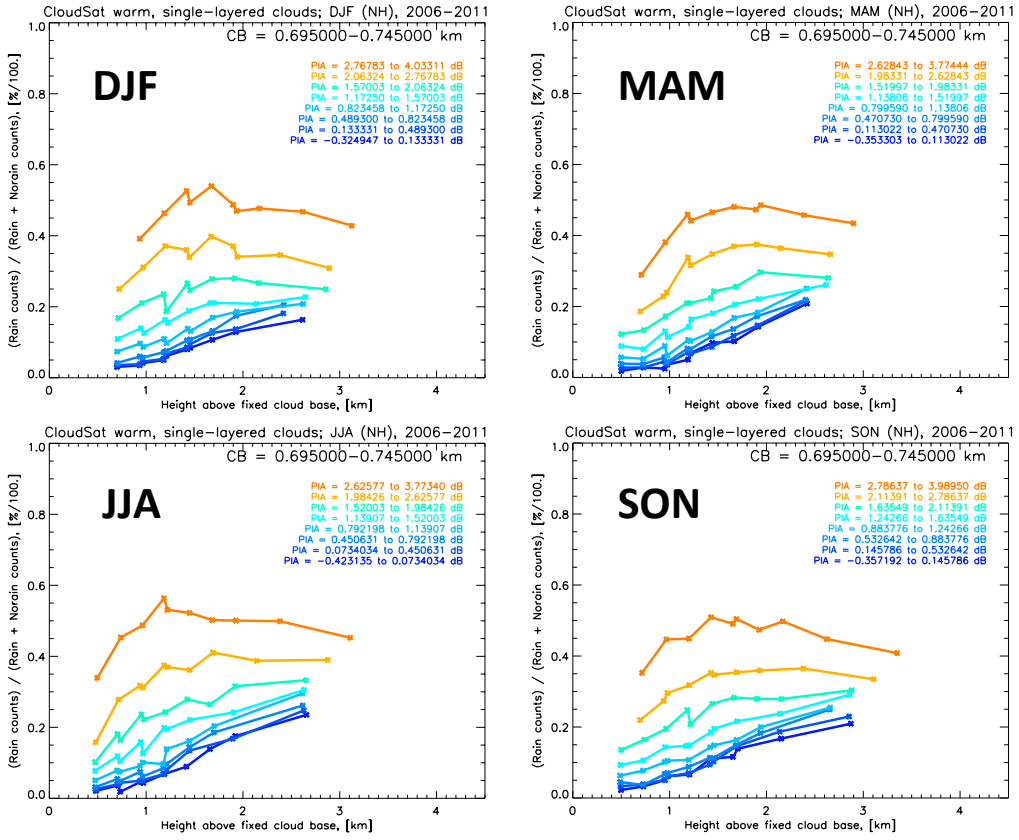

Figure 4.9. As in Figure 4.8a, but for CloudSat observations of warm clouds made throughout different seasons within the Northern Hemisphere.

Recall from Section 2.4 that SST within the RAMS simulation was fixed at 300 K. The SSTs associated with the observed warm cloud distribution, on the other hand, span a much wider range on either side of 300 K. Indeed, the 10th and 90th SST percentile values within the CloudSat warm, single-layered cloud data set are approximately 285 and 301 K, respectively. To assess the relative importance of this physical environmental difference on the CloudSat-RAMS differences discussed in Section 4.3, ancillary SST data from the ECMWF-AUX product were used to constrain the CloudSat distribution to those warm, single-layered clouds associated with underlying SST values of 300 ± 0.25 K. Not surprisingly, this additional screening step does act to significantly reduce the overall size of the raining and non-raining warm cloud distribution. The overall percentage of raining scenes within this fixed SST subset is actually 4% higher than it is when SST is not constrained (Table 4.2), indicating that rain from warm clouds is moderately more likely when the underlying ocean surface is warmer, a result likely related to the increased availability of water vapor associated with higher SSTs [e.g., Stephens 1990]. The CloudSat warm rainfall occurrence trends first shown in Figure 4.8a were recalculated for this fixed SST subset (Figure 4.10). Again, the relationships derived from the constrained warm cloud subset closely resemble those derived from the entire observed warm cloud distribution. Moreover, while SSTs within this observational subset are identical to those within the RAMS simulation, rainfall occurrence as a function of PIA and cloud depth within this CloudSat subset is not more similar to the RAMS-derived trends in Figure 4.8b. Thus, we conclude that not constraining SST within the CloudSat warm cloud distribution does not significantly alter our understanding of the CloudSat-RAMS rainfall occurrences discussed in Section 4.3.

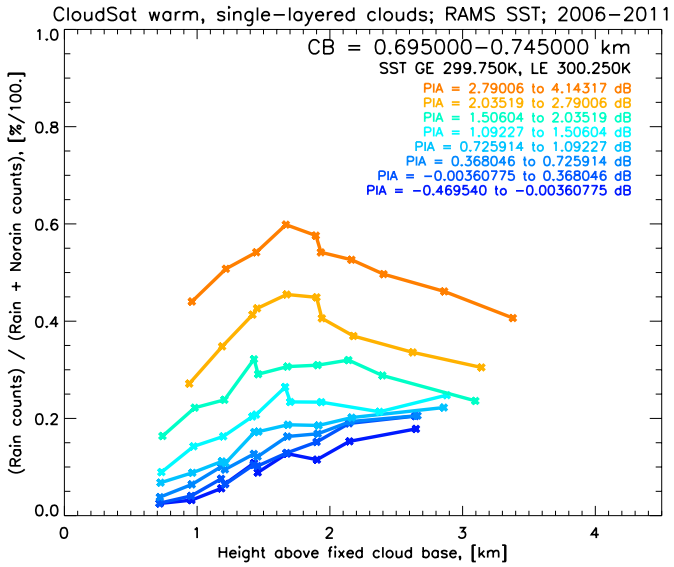

Figure 4.10. As in Figure 4.8a, but for CloudSat observations of warm clouds associated with underlying SST ≈ 300 K.

Also recall from Section 2.4 that the RAMS simulation analyzed within this study was initialized with a sounding characteristic of the mean tropical atmosphere. Thus, if the resulting warm clouds simulated with RAMS are, in fact, more characteristic of those existing within a tropical environment, one might suspect that the inclusion of observed warm clouds from outside of the tropics may bias the resulting modeled and observed rainfall occurrence relationship differences. To explore this possibility, the CloudSat warm, single-layered cloud distribution was constrained to observations made between 20°N and 20°S latitudes. The resulting tropical raining and non-raining observed warm cloud distributions are still large, and the overall fraction of raining clouds observed within these tropical latitudes is only marginally (~2%) higher than that characterizing 70°N - 70°S latitudes (Table 4.2). As the majority of the raining and non-raining observed warm cloud distributions stem from the tropics (Figure 3.3), this lack of major bulk statistical warm rainfall occurrence differences is to be expected. The relationships between cloud

macrophysical properties and warm rainfall occurrence for the observed tropical warm cloud subset are plotted in Figure 4.11. While largely comparable to the overall trends in Figure 4.8a, the decrease in rainfall likelihood with increasing cloud depth within the highest PIA percentile bin (darkest orange curve) is slightly more pronounced within this tropical data set; this trend is more in line with the RAMS-derived results in Figure 4.8b. However, as the application of this tropical constraint otherwise does not drastically alter our understanding of the model-observation differences discussed within Section 4.3, we conclude that the inclusion of observed warm clouds from outside the tropics within our CloudSat statistics does not bias the overall warm rainfall occurrence trends.

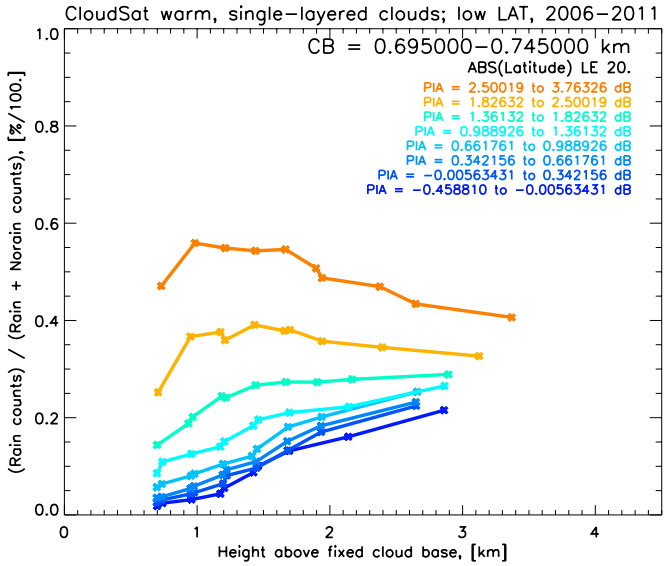

Figure 4.11. As in Figure 4.8a, but for CloudSat observations of warm clouds made over the tropical (20°N - 20°S) oceans.

The incoming solar radiation within the RAMS RCE simulation was fixed at a constant 450 W m^{-2} (Section 2.4). While this value was chosen because it is approximately equal to the time-integrated mean amount of incoming solar radiation at the equator, its use does not facilitate explicit representation of the full diurnal cycle within the simulation

(Igel and van den Heever 2013). CloudSat, on the other hand, crosses the equator at approximately 1:30 PM and 1:30 AM local time in the ascending and descending segments of its sun-synchronus orbit, respectively. Thus, while CloudSat does not capture the full diurnal cycle of warm clouds over the global oceans, it was conceivable that any day-night differences within the observed warm cloud distributions could influence the rainfall occurrence trends in Figure 4.8a. In using CloudSat observations to characterize precipitation from marine low clouds within the southeastern Pacific stratocumulus region, Rapp et al. (2013) stratified scenes within ascending and descending overpasses to show that approximately 75% of the total (day + night) raining cloudy scenes within the region of study were observed during nighttime overpasses. To investigate whether similar day-night rainfall differences exist on a more global scale and whether or not any such differences influence the RAMS-CloudSat rainfall occurrence differences discussed in Section 4.3, CloudSat warm cloudy scenes were separated into ascending and descending overpass groups. The resulting raining cloud counts (Table 4.2) indicate that approximately 61% of the total (day + night) raining clouds are observed during the nighttime, a ratio lower than that reported by Rapp et al. (2013) for the southeastern Pacific stratocumulus region. However, because more non-raining warm clouds are also identified during nighttime CloudSat overpasses, the resulting relative fraction of raining to total (raining and non-raining) warm, single layered clouds is very comparable during both daytime and nighttime (Table 4.2, final column). That is, while more raining clouds are identified during the nighttime than during the daytime over the global oceans, the relative proportion of the total warm clouds that are raining remains nearly equal during the day and night.

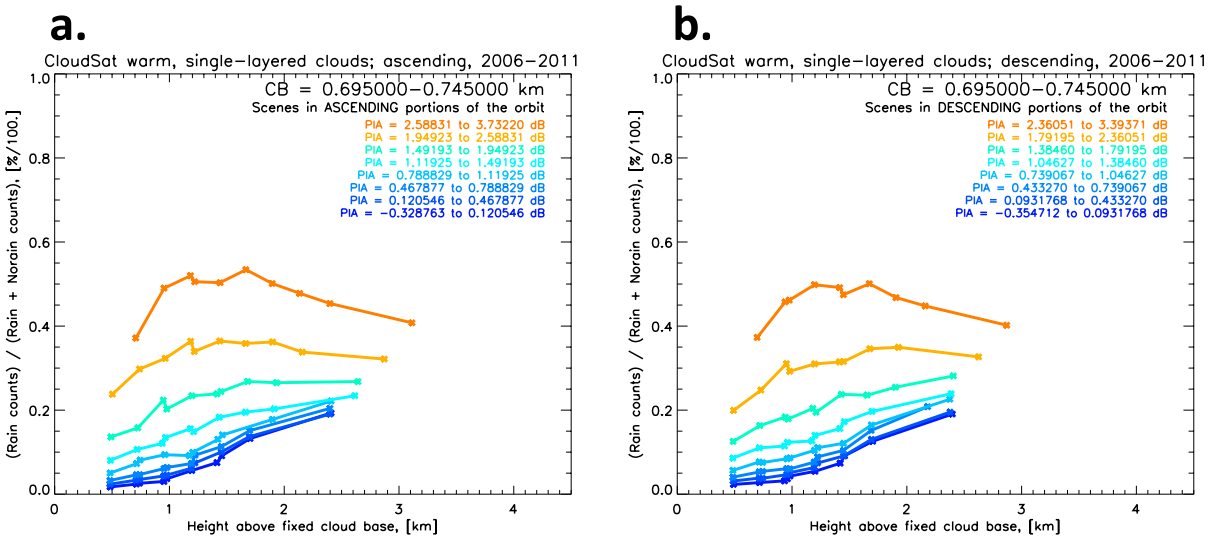

Figure 4.12. As in Figure 4.8a, but for CloudSat-observed warm clouds within (a) ascending and (b) descending CloudSat overpasses. Scenes within ascending and descending portions of the orbit characterize the day and night, respectively.

The fractional occurrences of warm rainfall as a function of cloud depth, stratified by PIA are shown for warm clouds within ascending (daytime) and descending (nighttime) CloudSat overpasses in Figures 4.12a and 4.12b, respectively. The day and night warm rain occurrence trends are very similar to both one another and to the overall warm cloud relationships in Figure 4.8a. For a given cloud depth, rain is increasingly more likely as PIA increases, regardless of the time of day. Moreover, for fixed PIA values below approximately 2 dB, the likelihood of warm rainfall increases with increasing cloud depth during both the daytime and the nighttime. Thus, while the overall number of warm clouds observed during nighttime CloudSat overpasses exceeds that observed during the daytime, the relationships between warm rain occurrence, cloud depth and PIA are consistent regardless of whether it is night or day.

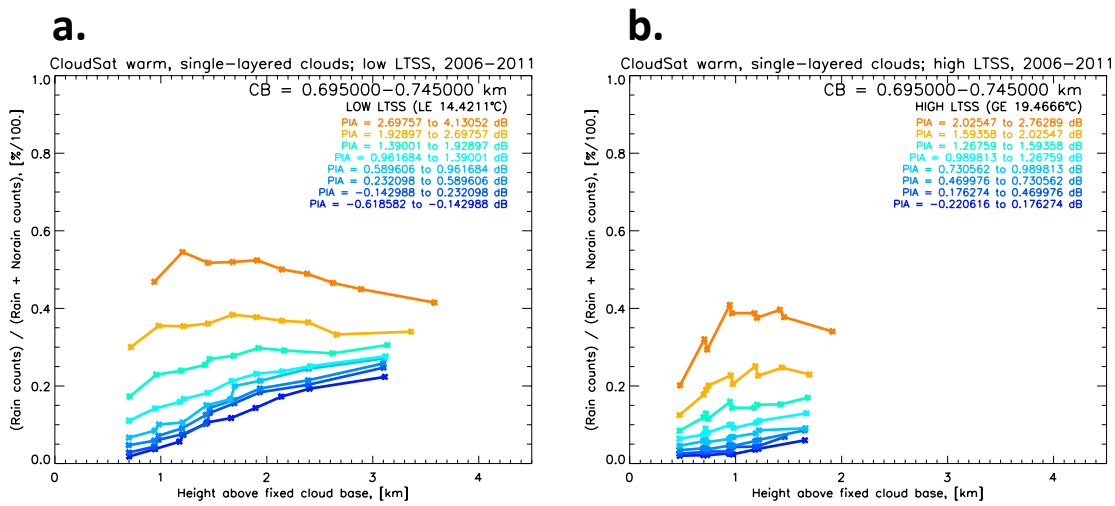

Figure 4.13. As in Figure 4.8a, but for CloudSat-observed warm clouds associated with lower tropospheric static stability (LTSS) values (a) below the 20th percentile value and (b) above the 80th percentile value. LTSS is defined as the potential temperature difference between 1000 and 700 mb pressure levels, and is calculated for each CloudSat scene using the ECMWF-AUX product.

To explore the influence of atmospheric thermodynamic state in these warm rainfall occurrence statistics, lower tropospheric static stability (LTSS) values were calculated from ancillary ECMWF-AUX reanalysis temperature fields as the potential temperature difference between the 700 and 1000 mb pressure levels. Using the same LTSS definition, Lebsock et al. (2008) and L'Ecuyer et al. (2009) showed that CloudSat-identified warm clouds within more stable (high LTSS) environments were more likely to rain at lower CWPs, as the same column water mass confined to the shallower cloud layers found in these stable environments lead to higher water mass concentrations and efficient warm rain processes. In the present analysis, the calculated LTSS distribution was used to separate stable environments (LTSS values above the 80th percentile value of ~19.5°C) from unstable environments (LTSS values below the 20th percentile value of ~14.4°C). All else remaining variable, warm clouds within unstable environments are much more likely to produce rainfall than those forming within stable environments (Table 4.2). Figures

4.13a and 4.13b show the fractional occurrence of rainfall as a function of cloud depth, stratified by PIA for warm clouds within these unstable and stable environments, respectively. These figures indicate that warm clouds within stable environments are characterized by lower PIA values and shallower cloud depths than clouds forming within unstable environments. While the curious increasing rainfall probabilities with increasing cloud depths within the lowest PIA percentile bins are more pronounced for warm clouds within unstable environments (Figure 4.13a), they are still evident for the stable subset of warm clouds (Figure 4.13b).

In summary, while some of the additional stratifications applied to the CloudSat data within this subsection did act to modify the relative sizes of the observed raining and non-raining warm cloud distributions, none of the screening procedures resulted in cloud macrophysical property-warm rain occurrence relationships that were drastically different from those characterizing the overall CloudSat trends in Figure 4.8a. Moreover, despite applying additional screening steps designed to make the CloudSat and RAMS warm cloud distributions more directly comparable (fixed SST; tropical regions only), the resulting observed warm rain occurrence trends within these observational subsets did not come any closer to resembling those derived from RAMS (Figure 4.8b) and, thus, did not act to resolve the CloudSat-RAMS differences discussed in Section 4.3.

4.4 Towards better understanding cloud life cycle

Cumulus cloud life cycle is often conceptualized as consisting of three distinct steps: growth, maturity, and dissipation (e.g., Malkus 1952; Byers and Hall 1955; Heus et al. 2009; Witte et al. 2013). Within this construct, incipient clouds increase in depth through their

growth stage, cease growth and precipitate any rain hydrometeors they have managed to develop during their mature phase, and break apart due to factors such as water mass rain out and/or entrainment in their dissipation stage. Thus, while the production of rainfall from warm clouds in this simple view is related to cloud depth – and, by association, CWP or PIA (Figure 4.6) – it is ultimately dependent upon another critical, and perhaps all encompassing, factor: time. As all of the CloudSat and RAMS composite cloud macrophysical-rainfall occurrence relationships discussed within previous sections were derived from many individual "snapshot" images of real and simulated warm clouds, they are inherently representative of the collective amount of time clouds exist within these various life stages. Here, we explore whether any differences in the evolution of modeled and observed warm clouds through these life stages could account for the differences in RAMS-simulated and CloudSat-observed rainfall occurrence statistics discussed within Section 4.3.

In a study aimed at better characterizing CloudSat observations of cumulus congestus clouds over the tropical oceans, Luo et al. (2009) developed a methodology that provided a more dynamic context for snapshot images of deep convective clouds. The concept was based upon assessing whether the tops of clouds were, at the time of observation, positively or negatively buoyant relative to their surrounding environment. Positively buoyant ("transient") clouds, those with cloud-top temperatures (CTT) warmer than the environmental temperature at the same height (T_{env}), were interpreted to have been actively growing when observed; negatively buoyant ("terminal") clouds were more likely to have already ceased their vertical development. In light of the conceptual ideas of cloud life cycle discussed at the beginning of this section, positively and negatively buoyant

clouds most likely represent growing and mature/dissipating clouds, respectively. To calculate cloud-top temperature differences, Luo et al. made use of collocated A-Train observations and ECMWF reanalysis data. Cloud-top height measurements from CloudSat were used in conjunction with ECMWF-AUX environmental temperature profiles to determine T_{env}. Collocated MODIS brightness temperatures were then used to calculate CTT for each CloudSat-identified deep convective cloud, under the assumption that actual CTTs were 6 K cooler than these brightness temperatures would suggest. Based upon the resulting histogram of cloud-top temperature differences (Figure 4.14), the authors estimated that approximately 30-40% of the cumulus congestus-like clouds observed in snapshot views from CloudSat were positively buoyant at cloud-top, and, thus, likely continued to develop into deeper convection after the observations were made. While deep convection is not the focus of the present study, Luo et al. (2009) suggested that the same methodology could also be used to provide additional insight into the nature of observed shallow convection.

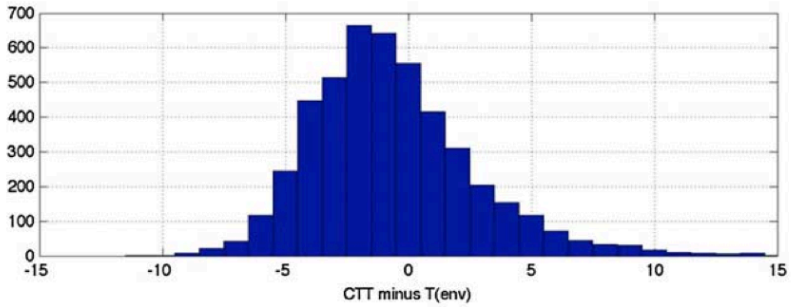

Figure 4.14. Histogram of the difference between MODIS-derived cloud-top temperature (CTT) and the ECMWF-AUX environmental temperature at the same height (T_{env}) for CloudSat-identified oceanic cumulus congestus clouds. From Luo et al. (2009).

The methodology used to assess warm cloud maturity within the present study closely resembles that of Luo et al. (2009). However, in comparison to the cloud-top

temperature differences characterizing the more convective cumulus congestus clouds examined within the previous study, the magnitude of the same temperature differences were expected to be significantly smaller for the warm clouds explored within the present study, potentially bordering upon the magnitude of the uncertainties in the observationally-based methodology itself. Thus, instead of directly applying the same procedure outlined by Luo et al. (2009) to warm clouds observed by CloudSat, a similar cloud-top buoyancy analysis was carried out only for RAMS-simulated warm clouds. For each warm, single-layered RAMS cloud identified through the procedures outlined in Section 3.3, CTT was simply defined as the temperature at the analyzed cloud-top height. The corresponding T_{env} for each of these clouds was then calculated by averaging non-cloudy model temperatures for grid boxes at the same cloud-top altitude within a 15 km^2 "box" surrounding the cloud of interest. The size of this box was chosen as a compromise to obtain a representative estimate T_{env} in the immediate vicinity of the simulated warm clouds while minimizing data reduction due to complete cloud contamination. Using a 15-km^2 search box, the T_{env} estimates were calculated from an average of approximately 56 neighboring non-cloudy model grid points.

The resulting histogram of cloud-top temperature differences in Figure 4.15 indicates that the majority of the warm, single-layered clouds identified from the RAMS simulation are actually cooler than their surrounding environments, or negatively buoyant, at cloud-top. Positively buoyant clouds account for only 22% of the entire RAMS warm, single-layered cloud distribution. In itself, this result may imply that warm clouds within the RAMS simulation rapidly lose any initial positive buoyancy that they possess within their incipient stages.

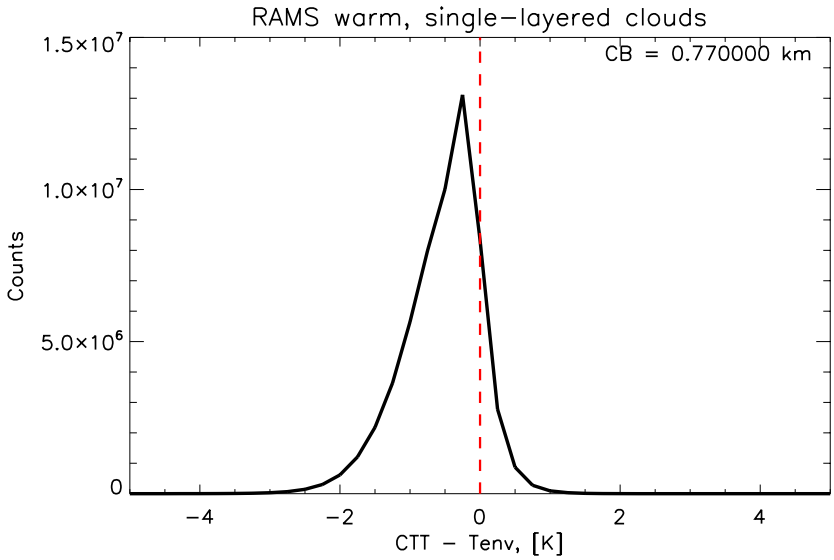

Figure 4.15. Histogram of the temperature difference between cloud-top (CTT) and the surrounding cloud-free environment at the same height (T_{env}) for RAMS-simulated warm, single-layered clouds with fixed cloud base heights.

The likelihood of rainfall from warm clouds simulated with RAMS is related to cloud-top buoyancy (Figure 4.16). Namely, rainfall is most probable from the simulated warm clouds that are most negatively buoyant at cloud-top. Physically, this result is in line with the conceptual view of cloud life cycle outlined at the beginning of this section. While positive cloud-top buoyancy is expected to be a characteristic of developing warm clouds, negative cloud-top buoyancy is more likely an attribute of mature or dissipating clouds (i.e., those that developed with some initial buoyancy that was then lost over time). Thus, that simulated warm rainfall occurs more often in association with negative cloud-top buoyancy may also imply that rain is more likely to fall from mature or decaying warm clouds than from those that are still within their growth stage.

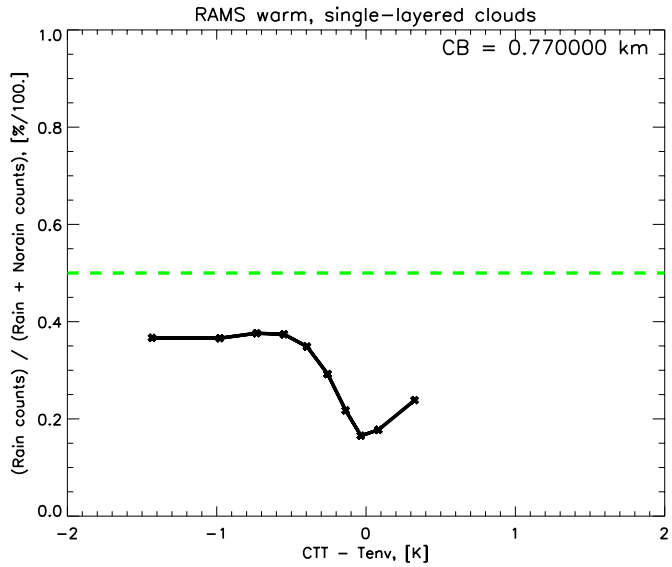

Figure 4.16. Fractional occurrence of warm rainfall as a function of the temperature difference between CTT and T_{env} for RAMS-simulated warm, single-layered clouds with fixed cloud base heights.

In light of these results and associated ideas on cloud life cycle, the cloud layer attenuation-warm rainfall occurrence trends explored within Section 4.3 were revisited. Similar to the experiments involving subsets of the entire CloudSat warm cloud distribution within Section 4.3.1, the intent was to examine whether or not the general RAMS warm rainfall occurrence trends in Figure 4.8b held when the analysis was restricted to the high- and low-end tails of the cloud-top buoyancy distribution (Figure 4.15). The 10% least buoyant warm clouds within the RAMS distribution, those characterized by CTTs ~ 1.2 K or more cooler than their surrounding environment, were subset first. The resulting relationships between cloud macrophysical properties and rainfall occurrence for these negatively buoyant simulated warm clouds are shown in Figure 4.17. These trends largely mirror the general RAMS warm cloud trends in Figure 4.8b. For any given cloud depth, rain is increasingly more likely with increasing PIA values. Moreover, for any given fixed PIA value, rain generally becomes less likely – or, in the case of the lowest PIA

percentile bins, remains equally as unlikely – with increasing cloud depth. Collectively, these results indicate that the likelihood of rainfall from these negatively buoyant warm clouds is generally dictated by the availability of liquid water, a characteristic that likely promotes active warm rain processes. As the majority of the clouds within the entire RAMS warm, single-layered cloud distribution were negatively buoyant at cloud-top (Figure 4.15), perhaps it is no surprise that rainfall occurrence trends from these negatively buoyant clouds should so closely mirror those from the general warm cloud case.

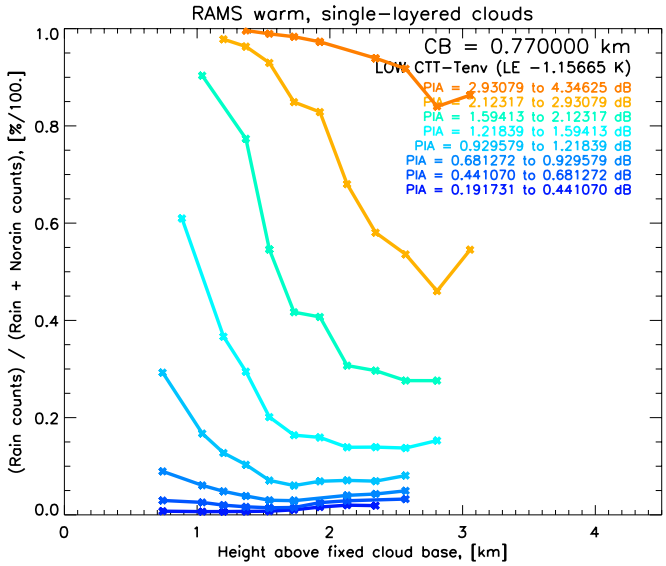

Figure 4.17. As in Figure 4.8b, but for the 10% least buoyant RAMS-simulated warm clouds.

The same rainfall occurrence trends characterizing the most positively buoyant simulated warm clouds display features more characteristic of the CloudSat-derived trends in Figure 4.8a. The RAMS warm cloud distribution was first restricted to the 10% most buoyant clouds, those with CTTs ~ 0.2 K or more warmer than their surrounding environments. The resulting relationships between PIA, cloud depth, and warm rain likelihood for this positively buoyant warm cloud subset are shown in Figure 4.18a. Similar to the trends derived from all RAMS warm, single-layered clouds, rainfall from warm

clouds of the same depth is still increasingly more likely as PIA increases, and for the highest PIA percentile bins, rainfall likelihood still decreases with increasing cloud depth. However, within the lowest PIA percentile bins, rain is modestly more likely with increasing cloud depth. For example, for PIA ranging between ~ 0.4 and 0.6 dB (second darkest blue curve), rain likelihood increases from ~ 1 to 6.5% as warm cloud depth increases from 1 to 2 km. When the distribution is further constrained to the 2.5% and 1% most positively buoyant warm clouds (CTTs ~ 0.5 and 0.7 K or more warmer than their surrounding environments, respectively), increasing rainfall likelihood with cloud depth within the lowest PIA percentile bins is even more pronounced (Figures 4.18b and 4.18c). For warm clouds with PIA values between ~ 0.4 and 0.8 dB (second darkest blue curve) within the 1% most buoyant cloud subset (Figure 4.18c), the probability of rainfall increases from ~ 6 to 30% as cloud depth increases from 1 to 2 km.

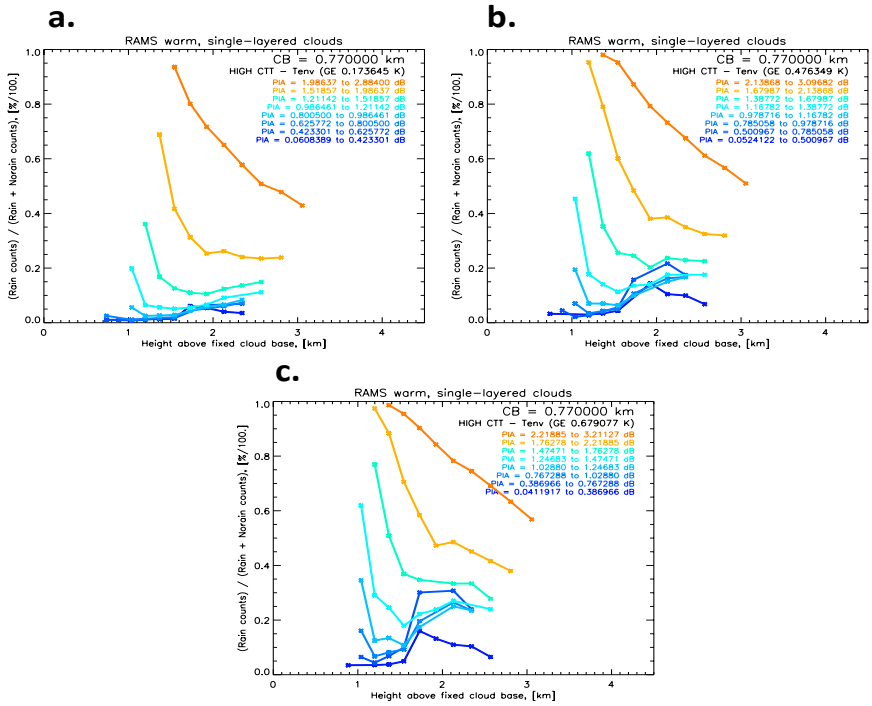

Figure 4.18. As in Figure 4.8b, but for the (a) 10%, (b) 2.5% and (c) 1% most buoyant RAMS-simulated warm clouds.

The positively buoyant RAMS warm rainfall occurrence trends in Figure 4.18 are decidedly more reminiscent of the comparable CloudSat-derived relationships in Figure 4.8a. For both sets of warm clouds, the probability of rainfall within the lowest PIA percentile bins generally increases as a function of cloud depth. Within higher PIA percentile bins, the observed and modeled rainfall likelihood trends might not be as dissimilar as they first appear. For the highest observed PIA percentile bin in Figure 4.8a (darkest orange curve), rainfall does become increasingly less likely as cloud depths increase, though this decrease is not as dramatic as is suggested by the RAMS-derived trends in Figure 4.18. Collectively, these results imply that warm clouds observed by CloudSat spend more time in their growth stage than those simulated with RAMS. That the majority of RAMS-simulated warm clouds are negatively buoyant at cloud-top may suggest that these clouds mature – and produce rainfall – too quickly relative to clouds observed in reality. The latter conclusion may have been foreshadowed within Section 4.1, where it was shown that RAMS-simulated warm clouds rain more often at lower PIA values than was suggested by CloudSat observations (Figures 4.2 and 4.3a). While this finding supported the idea that cloud water was too quickly converted to rain water within RAMS (Suzuki et al. 2011), it might also support the notion that the production of rainfall within RAMS is accelerated in time. The observed and simulated warm cloud PIA distributions themselves also support this idea. That the median observed PIA value within the 95^{th} – 100^{th} percentile bin is double that of the comparable simulated value again implies that RAMS clouds are more likely to rain out their water mass before attaining the higher PIA values observed within the CloudSat distribution.

In light of this understanding, the largely counterintuitive observed warm rainfall occurrence relationships discussed in Section 4.3 begin to make more physical sense. For the lowest PIA percentile bins, CloudSat-observed warm rainfall became increasingly more likely with increasing cloud depth, which seemingly implied that clouds with lower mean in-cloud averaged TWC (Figure 4.7) were actually more likely to produce rainfall. However, the cloud-top buoyancy analysis summarized within this section suggests that these rainfall trends characterize positively buoyant, developing warm clouds. If clouds are positively buoyant and, thus, growing in time, then perhaps deeper growing clouds with similar, or even slightly higher, PIA values as their shallower counterparts have simply had more time to produce rainfall. When warm clouds contain large amounts of liquid water (high PIA), the greater availability of liquid water likely promotes vigorous warm rain processes, which act to more efficiently convert cloud water to rain water. In the latter case, the amount of time necessary to produce warm rainfall may be shortest when the same amount of liquid water is confined to a shallower cloud layer (highest mean in-cloud averaged TWC), increasing with deeper clouds (lower mean in-cloud averaged TWC) thereafter.

CHAPTER 5: SUMMARY AND DISCUSSION

Modeled and observed warm rain occurrence and its bulk statistical relationships with cloud macrophysical properties have been analyzed. It was found that CloudSat-observed and RAMS-simulated warm clouds were increasingly more likely to produce rainfall when they contained greater amounts of column-integrated water mass within their volumes. However, warm clouds simulated with RAMS produced rain more frequently at lower PIA than was suggested by CloudSat observations. Warm rain within RAMS was statistically more likely than not at a PIA of 2 dB, a point approximately 1 dB lower than was observed. In line with the findings of Suzuki et al. (2011), this result suggested that the parameterized cloud-to-rain conversion processes within RAMS produce rainfall too efficiently.

It was also shown that modeled and observed warm rain was more likely to fall from deeper clouds. This increase was slightly more pronounced in the RAMS data set; the deepest simulated warm clouds (3-km deep) were approximately 30% more likely to produce rain than their observed counterparts. Further investigation revealed that deeper clouds were associated with higher mean PIA values, which suggested that the increased availability of liquid water preferentially supports more active warm rain processes within clouds of the greatest vertical extent.

The finding that PIA and cloud depth were directly related to one another and that increases in both were associated with greater probabilities of rainfall was not wholly unexpected. However, when rainfall probabilities were calculated simultaneously as a joint function of PIA and cloud depth, dramatic model-observation differences between rainfall

occurrence and cloud-mean TWC were discovered. Within RAMS, rainfall likelihood was found to be largely, and intuitively, governed by water availability. Simulated warm rain was statistically most probable when a large amount of liquid water was confined to a shallow cloud layer, as this combination resulted in the highest cloud-mean TWC and, thus, supported efficient warm rain coalescence processes. The same relationships derived from CloudSat observations were more complex. While water availability was certainly one factor that determined a real warm cloud's propensity to produce rainfall, another intervening factor seemed equally as critical when PIA was low. For observed clouds characterized by the same low PIA, rainfall probability increased with increasing cloud depth, despite decreasing cloud-mean TWC.

Better understanding the latter counterintuitive CloudSat result was the focus of the rest of this study. Many potentially feasible causes for this behavior were ruled out. The rainfall occurrence trends did not come closer to resembling those derived from RAMS when observational constraints were applied to improve model-observation comparability. Moreover, the observed relationships varied little when stratified by season and ascending (day) and descending (night) overpass groups. Focus was then shifted to better understanding how cloud maturity could be influencing these composite rainfall probability relationships. To this author's knowledge, the ensuing initiative represented the first time warm rain occurrence had been quantitatively investigated within the context of cloud life cycle. Using temperature differences between RAMS cloud tops and their immediate surrounding environment as a proxy for cloud-top buoyancy, it was shown that rainfall likelihoods for simulated clouds with tops warmer than their environments exhibited the same properties which characterized the overall CloudSat-derived trends.

Based on this finding, it was concluded that the CloudSat-observed warm cloud distribution was characterized by increased numbers of positively buoyant, developing clouds.

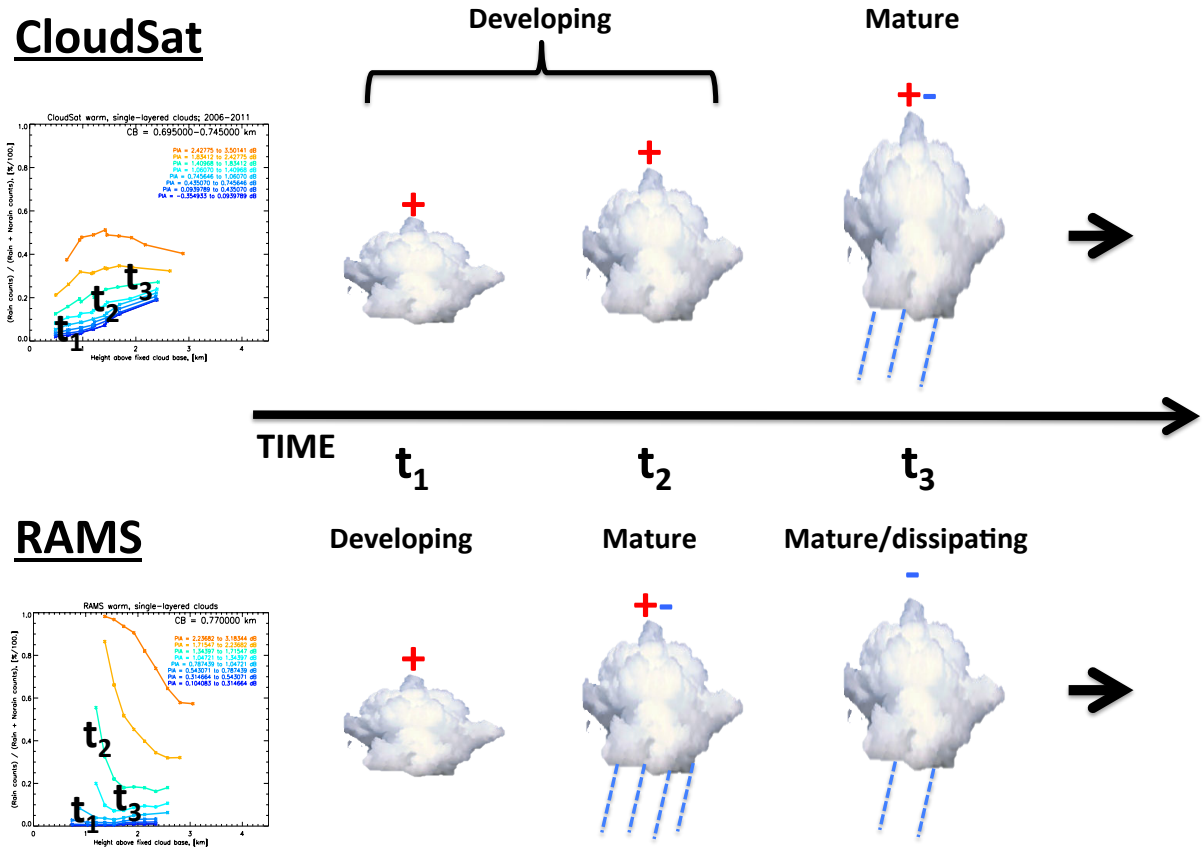

Figure 5.1. Schematic representation of proposed warm cloud evolution. Positive, neutral and negative cloud-top buoyancy are denoted by *+*, *+ –* and *–* symbols, respectively.

Based on these model-observation rainfall occurrence differences, a conceptual representation of the temporal evolution of real and simulated warm clouds was developed (Figure 5.1). In short, it is hypothesized that warm clouds within nature mature more gradually in time than do those simulated with RAMS. It is proposed that while increasing liquid water contents trigger the rapid development of rainfall within RAMS clouds, the same liquid water contents do not so readily support actual rain production. If these cloud distributions were sampled randomly, CloudSat would observe greater quantities of

developing (positively buoyant) cloud scenes than are represented within the comparable RAMS cloud distribution.

These results present a number of potential avenues for future research. The most obvious course of study would be to explore what other types of factors could influence these results. Within the model, atmospheric aerosol concentrations could be modified to explore the relative magnitude of the hypothesized second aerosol indirect effect (Albrecht 1989). Recent observational studies have suggested that warm clouds developing in polluted marine environments require more liquid water mass to produce rainfall (Berg et al. 2008; Lebsock et al. 2008; L'Ecuyer et al. 2009; Kubar et al. 2009; Saleeby et al. 2010), though these results are reliant upon ancillary estimates of either aerosol properties or cloud microphysical variables and their associated uncertainties. Additional environmental factors (e.g., wind shear, entrainment) not explored within the present study could act to influence these warm rain occurrence statistics; the relative importance of these factors for the production of warm rain merits future study. It should be noted that preliminary results from the present study also indicate that modeled and observed warm clouds are much more likely to rain when greater percentages of their neighboring clouds are also raining. While this result may underscore the importance of cloud organization in these warm rain statistics, further study is also merited here.

While it is expected that the cloud-top temperature difference methodology used within this study should give a rough indication of the distribution of cloud maturity, the warm cloud life cycle ideas developed herein would greatly benefit from more direct measurements of cloud evolution. Within RAMS, a cloud-tracking algorithm (e.g., Dawe and Austin 2012; Witte et al. 2013) could be developed to trace the full life cycle of simulated

warm clouds and identify temporal rainfall onset. Methodologies designed to track cloud features observed by satellites in time are inherently hindered by the nature of the observations themselves. While it is conceivable that CloudSat observations of warm clouds could be combined with ancillary geostationary satellite data to track cloud features in time, the limited spatial and temporal resolutions of the latter data set may inhibit such efforts. Additional observational insight into warm cloud evolution may be better gained through the analysis of surface-based measurements.

From an observational perspective, the relationships between column-integrated water mass and warm rain occurrence derived within this study could be used to improve cloud-rain partitioning schemes for microwave sensors. These results support growing evidence that the probability of warm rain increases monotonically as a function of column-integrated water mass (Lebsock et al. 2008; L'Ecuyer et al. 2009; Kubar et al. 2009; Suzuki et al. 2011). Thus, it is perhaps advisable for microwave retrieval schemes to abandon CWP partitioning thresholds in favor of taking a more statistical, probability-based approach to partitioning total column water mass. Such a scheme could begin from retrieved, non-partitioned TWP and then use the pre-calculated rainfall occurrence likelihood at this TWP to estimate how much water likely exists as rain.

From a modeling perspective, it is less clear how warm rain production that is too rapid would act to influence the distributions and properties of other simulated cloud types. Warm clouds play a major role in pre-conditioning tropical environments for deeper convection (e.g., Kuang and Bretherton 2006; Rapp et al. 2011). Therefore, might increased warm rain production act to accelerate this pre-conditioning process within the model and support more rapid development of deep convection? The answer to such a question is

likely complex, but it could have major implications for the representation of cloud radiative forcing within models.

REFERENCES

Ackerman, A. S., and Coauthors, 2009: Large-Eddy Simulations of a Drizzling, Stratocumulus-Topped Marine Boundary Layer. *Monthly Weather Review*, **137 (3)**, 1083–1110.

Albrecht, B., 1989: Aerosols, cloud microphysics, and fractional cloudiness. *Science*, **245**, 1227–1230.

Albrecht, B., C. W. Fairall, D. W. Thomson, A. B. White, J. B. Snider, and W. H. Schubert, 1990: Surface-based remote sensing of the observed and the adiabatic liquid water content of stratocumulus clouds. *Geophys. Res. Lett.*, **17**, 89–92.

Arkin, P. A., 1979: The relationship between fractional coverage of high cloud and rainfall accumulations during GATE over the B-scale array. *Mon. Wea. Rev.*, **107**, 1382–1387.

Berg, W., T. L'Ecuyer, and S. van den Heever, 2008: Evidence for the impact of aerosols on the onset and microphysical properties of rainfall from a combination of satellite observations and cloud-resolving model simulations. *J. Geophys. Res.*, **113**, D14S23, doi:10.1029/2007JD009649.

Berg, W., T. L'Ecuyer, and J. M. Haynes, 2010: The distribution of rainfall over oceans from spaceborne radars. *J. Appl. Meteor. Climatol.,* **49**, 535–543.

Berry, E. X., and R. L. Reinhardt, 1974: An analysis of cloud drop growth by collection: Part I. Double distributions. *J. Atmos. Sci.*, **31**, 1814 – 1824.

Bony, S., and J. Dufresne, 2005: Marine boundary layer clouds at the heart of tropical cloud feedback uncertainties in climate models. *Geophys. Res. Lett.*, **32**, L20806, doi:10.1029/ 2005GL023851.

Byers, H., and R. Hall, 1955: A census of cumulus cloud height versus precipitation in the vicinity of Puerto Rico during the winter and spring of 1953–1954. *J. Meteor.*, **12**, 176–178.

Chen, R., Z. Li, R. J. Kuligowski, R. Ferraro, and F. Weng, 2011: A study of warm rain detection using A-train satellite data. *Geophys. Res. Lett.*, **38**, L04804, doi:10.1029/2010GL046217.

Christensen, M. W., G. L. Stephens, and M. D. Lebsock, 2013: Exposing biases in retrieved low cloud properties from CloudSat: A guide for evaluating observations and climate data, *J. Geophys. Res. Atmos.*, **118**, doi:10.1002/2013JD020224.

Cotton, W. R., and Coauthors, 2003: RAMS 2001: Current status and future directions. *Meteor. Atmos. Phys*., **82**, 5–29.

Darby, Lisa S., Robert M. Banta, Roger A. Pielke, 2002: Comparisons between Mesoscale Model Terrain Sensitivity Studies and Doppler Lidar Measurements of the Sea Breeze at Monterey Bay. *Mon. Wea. Rev.*, **130**, 2813–2838.

Dawe, J. T., and P. H. Austin, 2012: Statistical analysis of an LES shallow cumulus cloud ensemble using a cloud tracking algorithm. *Atmos. Chem. Phys*., **12**, 1101–1119, doi:10.5194/acp-12- 1101-2012, 2012. 23463, 23475

Feingold, G., R. L. Walko, B. Stevens, and W. R. Cotton, 1998: Simulations of marine stratocumulus using a new microphysical parameterization scheme. *Atmos. Res*., **47–48**, 505–528.

Frisch, A. S., C. W. Fairall, and J. B. Snider, 1995: Measurement of stratus cloud and drizzle parameters in ASTEX with a Ka-band Doppler radar and a microwave radiometer. J. *Atmos. Sci*., **52**, 2788–2799.

Grabowski, W. W., 1998: Toward cloud resolving modeling of large-scale tropical circulations: A simple cloud microphysics parameterization. *J. Atmos. Sci*., **55**, 3283–3298.

Hartmann, D. L., M. E. Ockert-Bell, and M. L. Michelsen, 1992: The effect of cloud type on earth's energy balance - Global analysis. *J. Climate,* **5**, 1281–1304.

Haynes, J. M., and G. L. Stephens, 2007: Tropical oceanic cloudiness and the incidence of precipitation: Early results from CloudSat. *Geophys. Res. Lett.,* **34**, L09811, doi:10.1029/ 2007GL029335.

Haynes, J. M., R. T. Marchand, Z. Luo, A. Bodas-Salcedo, and G. L. Stephens, 2007: A multipurpose radar simulation package: QuickBeam. *Bull. Amer. Meteor. Soc*., **88**, 1723–1727.

Haynes, J. M., T. S. L'Ecuyer, G. L. Stephens, S. D. Miller, C. Mitrescu, N. B. Wood, and S. Tanelli, 2009: Rainfall retrieval over the ocean with spaceborne W-band radar. *J. Geophys. Res*., **114**, D00A22, doi:10.1029/2008JD009973.

Heus, T., H. J. J. Jonker, H. E. A. V. den Akker, E. J. Griffith, M. Koutek, and F. H. Post, 2009: A statistical approach to the life cycle analysis of cumulus clouds selected in a virtual reality environment. *J. Geophys. Res*., **114**, D06208, doi:10.1029/2008JD010917

Hilburn, K. A., and F. J. Wentz, 2008: Intercalibrated passive microwave rain products from the unified microwave ocean retrieval algorithm (UMORA). *J. Appl. Meteor. Climatol*., **47**, 778–794.

Igel, M. R., and S. C. van den Heever, 2013: The effects of domain size on the simulation of radiative-convective equilibrium. Accepted pending revision at *J. Atmos. Sci.*

Im, E., S. L. Durden, and C. Wu, 2005: Cloud Profiling Radar for the CloudSat mission. *IEEE Aerosp. Electron. Syst.*, **20**, 15–18.

Jonas, P. R., 1996: Turbulence and cloud microphysics. *Atmos. Res.*, **40**, 283–306.

Kessler, E., 1969: *On the Distribution and Continuity of Water Substance in Atmospheric Circulation. Meteor. Monogr.,* No. 32, Amer. Meteor. Soc., 84 pp.

Kuang, Z., and C. S. Bretherton, 2006: A mass-flux scheme view of a high-resolution simulation of a transition from shallow to deep cumulus convection. *J. Atmos. Sci.*, **63**, 1895–1909, doi:10.1175/JAS3723.1.

Kubar, T. L., D. L. Hartmann, and R. Wood, 2009: Understanding the importance of microphysics and macrophysics for warm rain in marine low clouds. Part I: Satellite observations. *J. Atmos. Sci.,* **66**, 2953–2972, doi:10.1175/2009JAS3071.1.

Kummerow, C. D., W. Barnes, T. Kozu, J. Shiue, and J. Simpson, 1998: The Tropical Rainfall Measuring Mission (TRMM) sensor package. *J. Atmos. and Oceanic Tech.*, **15**, 809-817.

Kummerow, C. D., and Coauthors, 2001: The evolution of the Goddard Profiling algorithm (GPROF) for rainfall estimation from passive microwave sensors. *J. Appl. Meteor.,* **40**, 1801–1820.

Kummerow, C. D., S. Ringerud, J. Crook, D. Randel and W. Berg, 2011: An observationally generated a-priori database for microwave rainfall retrievals, *J. Atmos. and Oceanic Tech.*, **28**, 113-130, doi: 10.1175/2010JTECHA1468.1.

Lau, K., and H. Wu, 2003: Warm rain processes over tropical oceans and climate implications. *Geophys. Res. Lett.*, **30**, 2290, doi:10.1029/2003GL018567.

Lebsock, M. D., G. L. Stephens, and C. Kummerow, 2008: Multisensor satellite observations of aerosol effects on warm clouds. *J. Geophys. Res.,* **113**, D15205, doi:10.1029/2008JD009876.

Lebsock, M. D., and T. S. L'Ecuyer, 2011: The retrieval of warm rain from CloudSat. *J. Geophys. Res.*, **116**, D20209, doi:10.1029/ 2011JD016076.

Lebsock, M. D., T. S. L'Ecuyer, and G. L. Stephens, 2011: Detecting the ratio of rain and cloud water in low-latitude shallow marine clouds. *J. Appl. Meteor. Climatol.*, **50**, 419–432, doi:10.1175/ 2010JAMC2494.1.

L'Ecuyer, T. S., and G. L. Stephens, 2002: An estimation-based precipitation retrieval algorithm for attenuating radars. *J. Appl. Meteor*., **41**, 272–285, doi:10.1175/1520-0450.

L'Ecuyer, T. S., W. Berg, J. Haynes, M. Lebsock, and T. Takemura, 2009: Global observations of aerosol impacts on precipitation occurrence in warm maritime clouds. *J. Geophys. Res.,* **114**, D09211, doi:10.1029/2008JD011273.

Leon, D. C., Z. Wang, and D. Liu, 2008: Climatology of drizzle in marine boundary layer clouds based on 1 year of data from CloudSat and Cloud-Aerosol Lidar and Infrared Pathfinder Satellite Observations (CALIPSO). *J. Geophys. Res.,* **113**, D00A14, doi:10.1029/2008JD009835.

Liu, Y., and P. H. Daum, 2004: Parameterization of the autoconversion process. Part I: Analytic formulation of the Kessler-type parameterizations, *J. Atmos. Sci*., **61**, 1539–1548.

Liu, C., and E. J. Zipser, 2009: "Warm Rain" in the Tropics: Seasonal and Regional Distributions Based on 9 yr of TRMM Data. *J. Climate*, **22**, 767–779.

Lovejoy, S., and G. L. Austin, 1979: The delineation of rain areas from visible and IR satellite data for GATE and mid-latitudes. *Atmos.–Ocean*, **17**, 77–92.

Luo, Z., G. Y. Liu, G. L. Stephens, and R. H. Johnson, 2009: Terminal versus transient cumulus congestus: A CloudSat perspective. *Geophys. Res. Lett*., **36**, L05808, doi:10.1029/2008GL036927.

Mace, G. G., R. Marchand, Q. Zhang, and G. Stephens, 2007: Global hydrometeor occurrence as observed by CloudSat: Initial observations from summer 2006. *Geophys. Res. Lett*., **34**, L09808, doi:10.1029/2006GL029017.

Malkus, J. S., 1952: The slopes of cumulus clouds in relation to external wind shear. *Q. J. R. Meteorol. Soc*., **78**(338), 530 – 542, doi:10.1002/ qj.49707833804.

Manton, M. J., and W. R. Cotton, 1977: Parameterization of the atmospheric surface layer. *J. Atmos. Sci.,* **34,** 331–334.

Marchand, R., G. G. Mace, T. Ackerman, and G. Stephens, 2008: Hydrometeor detection using CloudSat—An earth-orbiting 94 Ghz cloud radar. *J. Atmos. Oceanic Technol*., **25**, 519–533, doi:10.1175/ 2007JTECHA1006.1.

Matrosov, S. Y., 2007: Potential for attenuation-based estimations of rainfall rate from CloudSat. *Geophys. Res. Lett*., **34**, L05817, doi:10.1029/ 2006GL029161.

Medeiros, B., L. Nuijens, C. Antoniazzi, and B. Stevens, 2010: Low-latitude boundary layer clouds as seen by CALIPSO, *J. Geophys. Res*., **115**, D23207, doi:10.1029/2010JD014437.

Meyers, M. P., R. L. Walko, J. Y. Harrington, and W. R. Cotton, 1997: New RAMS cloud microphysics parameterization. Part II. The two-moment scheme. *Atmos. Res.,* **45,** 3–39.

Mitrescu, C., T. L'Ecuyer, J. Haynes, S. Miller, and J. Turk, 2010: CloudSat Precipitation Profiling algorithm—Model description. *J. Appl. Meteor. Climatol*., **49**, 991–1003.

Nicholls, S., 1987: A model of drizzle growth in warm, turbulent, stratiform clouds. *Quart. J. Roy. Meteorol. Soc*., **113**, 1141–1170.

Nuijens, L., B. Stevens, and A. P. Siebesma, 2009: The environment of precipitating shallow cumulus convection, *J. Atmos. Sci*., **66(7)**, 1962–1979.

O'Dell, C. W., F. J. Wentz, and R. Bennartz, 2008: Cloud liquid water path from satellite-based passive microwave observations: A new climatology over the global oceans*. J. Climate*, **21**, 1721–1738.

Pawlowska, H., and J.-L. Brenguier, 2003: An observational study of drizzle formation in stratocumulus clouds for general circulation model (GCM) parameterizations. *J. Geophys. Res.,* **108**, 8630, doi:10.1029/2002JD002679.

Pielke, R. A., and Coauthors, 1992: A comprehensive meteorological modeling system—RAMS. *Meteor. Atmos. Phys*., **49**, 69–91.

Rapp, A. D., C. D. Kummerow, and L. Fowler, 2011: Interactions between warm rain clouds and atmospheric preconditioning for deep convection in the tropics. *J. Geophys. Res*., **116**, D23210, doi:10.1029/2011JD016143.

Rapp, A. D., M. D. Lebsock, and T. S. L'Ecuyer, 2013: Low cloud precipitation climatology in the southeastern Pacific marine stratocumulus region using CloudSat. *Environ. Res. Lett.*, **8**, 014027, doi:10.1088/1748-9326/8/1/014027.

Rauber, R. M., and Coauthors, 2007: Rain in Shallow Cumulus over the Ocean: The RICO campaign. *Bull. Amer. Meteor. Soc*., **88**, 1912–1928.

Reiche, C. H., and S. Lasher-Trapp, 2010: The minor importance of giant aerosol to precipitation development within small trade wind cumuli observed during RICO. *Atmospheric Research*, ***95*****(4)**, 386-399.

Rémillard, J., Kollias, P., Luke, E., & Wood, R., 2012: Marine Boundary Layer Cloud Observations in the Azores. *Journal of Climate*, ***25*****(21)**, 7381-7398.

Rogers, R. R., and M. K. Yau, 1989: *A Short Course in Cloud Physics*. 3rd ed. Pergamon, 293 pp.

Saleeby, S. M, and W. R. Cotton, 2004: A large-droplet mode and prognostic number concentration of cloud droplets in the Colorado State University Regional Atmospheric Modeling System (RAMS). Part I: Module descriptions and supercell test simulations. *J. Appl. Meteorol.* **43**, 182–195.

Saleeby, S. M., W. Berg, S. van den Heever, and T. L'Ecuyer, 2010: Impact of cloud-nucleating aerosols in cloud-resolving model simulations of warm-rain precipitation in the East China Sea*. J. Atmos. Sci*., **67**, 3916–3930.

Saleeby, S.M., and S.C. van den Heever, 2013: Developments in the CSU-RAMS Aerosol Model: Emissions, Nucleation, Regeneration, Deposition, and Radiation. Accepted pending revision at *J. Appl. Meteor. Climatol*.

Savic-Jovcic, V., and B. Stevens, 2008: The structure and mesoscale organization of precipitating stratocumulus*. J. Atmos. Sci.*, **65**, 1587–1605.

Schumacher, C., and R. A. Houze, 2000: Comparison of radar data from the TRMM satellite and Kwajalein oceanic validation site*. J. Appl. Meteor*., **39**, 2151–2164.

Short, D. A., and K. Nakamura, 2000: TRMM radar observations of shallow precipitation over the tropical oceans. *J. Climate*, **13**, 4107–4124.

Snodgrass, E. R., L. Di Girolamo, and R. M. Rauber, 2009: Precipitation characteristics of trade wind clouds during RICO derived from radar, satellite, and aircraft measurements, *J. Appl. Meteorol. Climatol*., **48**, 464–483, doi:10.1175/2008JAMC1946.1.

Stephens, G. L., 1978: Radiation profiles in extended water clouds. Part II: Parameterization schemes. *J. Atmos. Sci*., **35**, 2123– 2132.

Stephens, G. L., 1990: On the relationship between water vapor over the oceans and sea surface temperature. *J. Climate,* **3,** 634–645.

Stephens, G. L., and Coauthors, 2002: The CloudSat mission and the A-train. *Bull. Amer. Meteor. Soc*., **83**, 1771–1790.

Stephens, G. L., and J. M. Haynes, 2007: Near global observations of the warm rain coalescence process. *Geophys. Res. Lett*., **34**, L20805, doi:10.1029/2007GL030259.

Stephens, G. L., and C. D. Kummerow, 2007: The remote sensing of clouds and precipitation from space: A review. *J. Atmos. Sci.*, **64**, 3742-3765.

Stephens, G. L., and N. B. Wood, 2007: Properties of tropical convection observed by millimeter-wave radar systems. *Mon. Weather Rev*., **135**, 821–842.

Stephens, G. L., S. van den Heever, and L. Pakula, 2008: Radiative – convective feedbacks in idealized states of radiative – convective equilibrium. *J. Atmos. Sci.,* **65**, 3899 – 3916.

Stephens, G. L., and Coauthors, 2008: CloudSat mission: Performance and early science after the first year of operation. *J. Geophys. Res*., **113**, D00A18, doi:10.1029/2008JD009982.

Storer, R. L., and S. C. van den Heever, 2013: Microphysical processes evident in aerosol forcing of tropical deep convective clouds. *J. Atmos. Sci*., **70**, 430–446.

Suzuki, K., and G. L. Stephens, 2009: Relationship between radar reflectivity and the time scale of warm rain formation in a global cloud- resolving model. *Atmos. Res*., **92**, 411–419.

Suzuki, K., T. Nakajima, M. Satoh, H. Tomita, T. Takemura, T. Y. Nakajima, and G. L. Stephens, 2008: Global cloud-system-resolving simulation of aerosol effect on warm clouds. *Geophys. Res. Lett*., **35**, L19817, doi:10.1029/2008GL035449.

Suzuki, K., G. Stephens, S. van den Heever, and T. Nakajima, 2011: Diagnosis of the warm rain process in cloud-resolving models using joint CloudSat and MODIS observations*. J. Atmos. Sci*., **68**, 2655–2670.

van den Heever, S., and W. R. Cotton, 2004: The impact of hail size on simulated supercell storms*. J. Atmos. Sci*., **61**, 1596–1609.

van den Heever, S. C., G. L. Stephens, and N. B. Wood, 2011: Aerosol indirect effects on tropical convection characteristics under conditions of radiative-convective equilibrium. *J. Atmos. Sci.*, **68**, 699-718.

Wang, J. H., W. B. Rossow, T. Uttal, and M. Rozen- daal, 1999: Variability of cloud vertical structure during ASTEX observed from a combination of rawinsonde, radar, ceilometer, and satellite. *Monthly Weather Review*, **127 (10)**, 2484–2502.

Webb, M. J., and Coauthors, 2006: On the contribution of local feedback mechanisms to the range of climate sensitivity in two GCM ensembles. *Climate Dyn*., **27**, 17–38, doi:10.1007/s00382- 006-0111-2.

Wentz, F. J., 1990: *SBIR Phase II Report: West coast storm forecasting with SSM/I*. RSS Tech. Rep. 033190, 378 pp. [Available from Remote Sensing Systems, 1101 College Avenue, Suite 220, Santa Rosa, CA 95404.]

Wentz, F. J., and R. W. Spencer, 1998: SSM/I rain retrievals within a unified all-weather algorithm. *J. Atmos. Sci.,* **55,** 1613–1627.

Wilheit, T. T., 1986: Some comments on passive microwave measurement of rain, *Bull. Am. Meteorol. Soc*., **67**, 1226–1232.

Witte, M. K., P. Y. Chuang, and G. Feingold, 2013: On clocks and clouds. *Atmos. Chem. Phys. Discuss*., **13**, 23461-23490, doi:10.5194/acpd-13-23461-2013.

Wood, R., 2012: Stratocumulus clouds. *Mon. Wea. Rev*., **140**, 2373–2423.

Zuidema, P., E. R. Westwater, C. Fairall, and D. Hazen, 2005: Ship-based liquid water path estimates in marine stratocumulus. *J. Geophys. Res*., **110**, D20206, doi:10.1029/2005JD005833.

Zuidema, P., D. Painemal, S. De Szoeke, and C. Fairall, 2009: Stratocumulus cloud top height estimates and their climatic implications. *J. Climate*, **22**, 4652–4666.